A yak−enriched CD4 *ATF7IP*$^{+}$ subtype is associated with pulmonary endothelial stress resistance under hypoxia

Ruilin Zeng[1,3,7,#], Wei Fu[2,3,#], Qiang Zhang[4,#], Dawei Yu[5], Jiabo Wang[3], Meng Xu[2,3], Shi Yin[3], Wenhui Ji[2,3], Yan Xiong[3], Tserang-Donko Mipam[6], Jian Li[1,3], WangDui BaSang[4], Daoliang Lan[1,2,3,*]

[1]Key Laboratory of Qinghai-Tibetan Plateau Animal Genetic Resource Reservation and Utilization, Southwest Minzu University, Ministry of Education, Chengdu 610041, China

[2]Institute of Qinghai-Tibetan Plateau, Southwest Minzu University, Chengdu 610225, China

[3]College of Animal and Veterinary Sciences, Southwest Minzu University, Chengdu 610041, China

[4]Institute of Animal Husbandry and Veterinary Medicine, Xizang Autonomous Region Academy of Agricultural and Animal Husbandry Sciences, Lhasa 850004, China

[5]State Key Laboratory of Animal Genetics Breeding and Reproduction, Ministry of Agriculture and Rural Affairs, Institute of Animal Science, Chinese Academy of Agricultural Sciences, Beijing 100193, China

[6]College of Grassland Resources, Southwest Minzu University, Chengdu 610225, China

[7]School of Life Sciences, Zhengzhou University, Zhengzhou 450001, China

[*]Corresponding author: Daoliang Lan, landaoliang@163.com

[#]These authors contributed equally to this work[1]

[1] This work was supported by Science and Technology Plan Project of the Xizang Autonomous Region (XZ202502ZY0001), Key R&D Project of Tibet Autonomous Region: Breeding and Application Research of New Yak Strains in Tibet (XZ202501ZY0031), National Key Research and Development Program of China (2023YFD1801305), Science and Technology Project of Tibet Autonomous Region (GZKJ-003), Qinghai Provincial “Kunlun Talents” High-End Innovation and Entrepreneurship Talent Program (QHKLYC-GDCXCY-2024-325), China Agriculture Research System of MOF and MARA (CARS-37) and Southwest Minzu University Double World-Class Project (XM2023020).

Zoological Research

ABSTRACT

Elucidating the regulatory mechanisms underlying adaptation to high-altitude hypoxia remains a central challenge in genetics. Yaks are exquisitely adapted to the plateau ecosystem, where the lung plays a pivotal role in gas exchange and blood oxygen homeostasis. To explore the cellular composition and molecular regulatory networks of the lung under hypoxic conditions, we constructed a single-cell transcriptomic atlas of the lungs of yak, dzho and cattle. We identified 51 cell subtypes, including 13 novel subtypes predominantly enriched in T&NK cells. Through integration of interspecies differential analysis, pseudotime analysis, and SCENIC analyses, we identified a unique CD4 *ATF7IP*$^{+}$ subtype that is markedly enriched in yaks. This subtype exhibits a stepwise increase in abundance across cattle, dzhos and yaks, establishing it as a hallmark subtype associated with high-altitude adaptation in yak. Subsequent intercellular communication analysis revealed that the CD4 *ATF7IP*$^{+}$ subtype displayed the strongest ligand–receptor interactions with the pulmonary gCap endothelial subtype. We further demonstrate that GPI/AMF secreted by the CD4 *ATF7IP*$^{+}$ subtype likely interacts with its receptor gp78/AMFR. This AMFR-mediated signaling pathway appears to depend on PI3K phosphorylation to drive AKT activation, which helps suppress ROS accumulation while maintaining pulmonary gCap viability and survival during hypoxia. Furthermore, treatment with recombinant GPI/AMF protein under hypoxic conditions reproduced these protective effects and partially substituted for CD4 *ATF7IP*$^{+}$ co-culture. In conclusion, this study reveals a previously unrecognized pulmonary immune-endothelial axis that supports gCap cell stress resistance under hypoxia, providing potential molecular targets for the conservation of yak germplasm and selective breeding programs.

Keywords: Hypoxia adaptation; Yak; Lung; scRNA-seq; cell−cell interaction.

uncorrected proof

INTRODUCTION

For centuries, elucidating the molecular mechanisms underlying adaptation to high-altitude hypoxic environments has been a crucial scientific issue in the fields of evolution and genetics. The yak (*Bos grunniens*), an indispensable livestock species capable of surviving in high-altitude areas, exhibits remarkable adaptation to the harsh plateau environment characterised by cold, hypoxia, high altitude and intense ultraviolet radiation (Qiu et al., 2012). It is widely distributed across the high-altitude plateau and has unique mechanisms and pathways for adapting to hypoxic conditions at high altitudes. The dzho (also known as dzo) (*Bos grunniens*×*Bos taurus*), an interspecific F1 hybrid between female yak and male domestic cattle (*Bos taurus*) (Long et al., 2020), is similarly adapted to harsh ecological conditions. As an F1 hybrid between yaks and cattle, dzhos offer a unique, multi-dimensional research window for exploring the hybrid-associated intermediate molecular or cellular phenotypes and regulatory mechanisms that are associated with bovine adaptation to extreme environments. Elucidating the adaptive mechanisms of high-altitude mammals not only deepens our understanding of evolutionary patterns in extreme environments but also provides a theoretical basis for the prevention and treatment of hypoxia-related diseases.

As the lung is a primary target organ for studying high-altitude adaptability, this study focuses on the lung to explore the adaptability of yak to high-altitude hypoxia environments. In addition to gas exchange, mammalian lungs have functions such as maintaining organismal acid–base balance and blood reserve. They also act as a crucial immune barrier (Hurskainen et al., 2021). After a long period of natural and artificial selection, the lungs of yak and dzho have developed corresponding adaptive structures and physiological regulation mechanisms to adapt to low–oxygen environments. Compared with other cattle breeds from the plains, the physiological structure of the lungs of yak shows some adaptive changes (Wang et al., 2016), such as an increased number of alveoli per unit area, increased alveolar area and enhanced richness of

Uncorrected proof

pulmonary vessels, thereby enhancing the efficiency of blood oxygen exchange. In addition, the hypoxic environment of the highlands has promoted the vascular remodelling of the yak lungs, enhancing the vasodilatory and contractile capacities of their blood vessels (Maron et al., 2014; Wang et al., 2014).

Previous studies on the yak lung have largely focused on its unique histological architecture and morphological adaptations to high-altitude stress. While subsequent studies on DNA variants and key functional genes have further revealed the genomic and phenotypic diversity of this organ (Gao et al., 2022), a detailed characterization of the cellular heterogeneity and intercellular signaling networks within the yak lung remains limited. Therefore, our study constructed a comprehensive single-cell transcriptome atlas of the lungs of yak, dzho and cattle. We observed that the high-altitude hypoxic environment profoundly reshapes the cellular landscape of the yak lung, particularly within T&NK immune cells. Given the shared evolutionary ancestry of endothelial and immune lineages, their intimate crosstalk is fundamental to tissue homeostasis. Notably, we identified a robust interaction between a specific CD4 *ATF7IP*$^{+}$ subtype and the gCap capillary endothelial subtype. The gCap subtype, primarily localized to thicker alveolar septa, is recognized as a critical functional population essential for vascular homeostasis. It is closely associated with inflammatory responses and vascular remodeling, exhibiting a rapid proliferative capacity to repair injury. Based on these findings, we hypothesized that this immune-endothelial crosstalk serves as a regulatory hub, where adaptive immune signals modulate vascular remodeling to enhance oxygen transport efficiency. Subsequent functional experiments validated this regulatory potential, revealing a novel mechanism by which the CD4 *ATF7IP*$^{+}$ subtype modulates the gCap subtype, thereby enhancing gCap viability and survival, suppressing ROS accumulation, and potentially contributing to sustained vascular stability and angiogenesis under hypoxia. By linking immune regulation to vascular homeostasis, we propose immune−endothelial axis as a key driver potentially contributing to hypoxic adaptation in the yak lung. This study provides a

Uncorrected proof

comprehensive overview of the molecular characteristics of the yak lung and offers a valuable resource for the conservation of yak germplasm and the advancement of selective breeding programs.

MATERIALS AND METHODS

Collection of lung tissues from yak, dzho and cattle

The yaks and dzhos collected for the experiment were located in Hongyuan County, Aba Tibetan and Qiang Autonomous Prefecture, Sichuan Province, which is situated at latitude N31°51'−33°19" and longitude E101°51'−103°23", with an average elevation of 3600 m. The entire lungs of the yaks/dzhos were quickly removed after they had completed the slaughtering procedure. Following aseptic procedures, for each individual, lung tissue samples of 1 cm^3 in size were precisely collected using surgical scissors from 6 sampling points on both sides of the lung lobes (i.e. left anterior, left middle, left posterior, right anterior, right middle and right posterior lobes), located 5 cm from the lung apex (Supplemental Figure S1A), avoiding bronchial tubes and blood vessels as much as possible. A total of 3 yak samples (n=3) and 3 dzho samples (n=3) were collected, all aged between 3 and 4 years, and all were male. The same method was used to collect lung tissue samples from 3 cattle (n=3), aged between 3 and 4 years old, all male, from Tashui Town, Anzhou District, Mianyang City, Sichuan Province, which is located at latitude N31°23'−31°47" and longitude E104°05'−104°38", with an average elevation of 570 m. For each animal, lung tissue samples collected from 6 different sites were pooled for subsequent single-cell transcriptomic analysis.

Preparation of lung tissue for single-cell RNA sequencing

The steps for processing lung samples for single-cell transcriptome experiments followed strict aseptic and standardized operating procedures. Freshly obtained lung tissues were rinsed in pre-cooled (4 °C) PBS without calcium and magnesium in a sterile Petri dish to remove blood, and sterile dust-free paper was used to remove moisture from the tissue surface. Immediately, each piece of lung tissue was transferred separately

Uncorrected proof

to a freezing tube containing cell freezing medium (90% FBS and 10% DMSO) and thoroughly resuspended. Subsequently, the cryovials containing the lung tissues were transferred to a gradient cooling box filled with isopropanol. The gradient cooling box was completely buried in dry ice for 12 h, after which the cryovials were transferred to a −80 °C ultra-low temperature freezer for short-term storage.

All samples collected in this study were formally approved by the Animal Ethics Committee of Southwest Minzu University (No. SMU-202501235), and all samples originated from government-approved abattoirs and complied with relevant ethical and regulatory requirements.

Isolation of single cells from lung tissue

Lung tissues in cryovials were thawed in a 37 °C water bath and washed 3 times in RPMI 1640 medium. The lung tissues were finely minced into approximately 0.5 mm^3 fragments using sterile surgical scissors in RPMI 1640 medium. These fragments were digested at 37 °C for 30 min in 1 mg/mL Type I collagenase (MCE, #HY-E70005A), followed by 10 min of digestion at 37 °C in 0.25% trypsin-EDTA (Gibco, #25200056). Lastly, 10% foetal bovine serum (Gibco, #A5256701) was added to stop digestion. Lung tissue suspensions were filtered through a 40 μm cell strainer (Corning, #352340), and erythrocytes were removed with red blood cell lysis buffer (Invitrogen, #00-4333-57). Lung cells were resuspended in DPBS containing 2% foetal bovine serum, and the cell suspension was counted and stored for subsequent experiments.

Single-cell mRNA sequencing

The dead cells were removed from the cell suspension with the Dead Cell Removal Kit (Milteny Biotec, #130-090-101), and the single-cell transcriptome sequencing libraries were constructed using Chromium Single Cell 3' Reagent Kits (V3; 10×Genomics). In brief, the whole library construction process was divided into 3 steps: GEM Generation & Barcoding, Post GEM-RT Cleanup & cDNA Amplification and 3' Gene

uncorrected proof

Expression Library Construction. Finally, all libraries were subjected to quality control (Fragment Analyzer 2100, Agilent Technologies) and sequencing (Platform: Illumina NovaSeq 6000).

Data processing and downstream analysis

Transcripts were mapped to the corresponding reference genome using the 10×Genomics CellRanger software (version 3.1.0). For cattle and yaks, the ARS-UCD2.0 (cattle) and BosGru3.1 (yak) assemblies were utilized, respectively. Given the absence of a specific reference genome for the dzho (an F1 hybrid), its transcripts were mapped to the cattle reference genome (ARS-UCD2.0), which offers superior annotation and facilitates interspecies comparisons.

Read count matrices for each sample were generated by CellRanger counts, and the count data were imported into the Seurat R package (version 4.1.3) for QC of each library with the following QC criteria: nCount RNA>=1000, nFeature RNA>=200, log10GenesPerUMI>0.7 and mitochondrial content=<15%. DoubletFinder was used to remove doublets for downstream analysis.

To eliminate batch effects in scRNA-seq data, we performed mutual nearest neighbours (MNNs). Principal component analysis (PCA) was used for the dimensionality reduction algorithm, and shared nearest neighbour (SNN) was used for the clustering algorithm. Visualization of the clustering results for individual or grouped samples was performed using RunUMAP.

Cell type annotation

Cell populations were automatically annotated using the ‘SingleR’ package based on highly variable marker genes. Subsequently, the cell clusters were manually annotated into different cell types based on the results of the ‘SingleR’ annotation results, datasets from websites such as http://xteam.xbio.top/CellMarker/ and https://lungmap.net/, existing related literature and the biological functions of characteristic genes (the marker genes used for cell annotation are listed in Supplemental Table S3). Different cell types annotated

Uncorrected proof

were displayed on a two-dimensional uniform manifold approximation and projection (UMAP) plot using the 'DimPlot'. Visualisation of representative genes in each cell type was achieved through functions like 'DotPlot and 'VlnPlot' (Park and Jeoung, 2020). To statistically compare cell populations across species, cell-type proportions were calculated independently for each biological replicate. Statistical differences in these proportions across yak, dzho, and cattle were evaluated using a one-way analysis of variance (ANOVA) based on the individual animals (n=3 per species).

GO, KEGG and GSVA analyses

Differentially expressed genes (DEGs) were identified using the FindAllMarkers function in the Seurat package (Wilcoxon rank-sum test). For all single-cell differential expression analyses, statistical significance was strictly determined using adjusted *P* values (false discovery rate, FDR) calculated via the Benjamini-Hochberg procedure, with a significance threshold of FDR<0.05. To avoid pseudoreplication, subsequent downstream evaluations, including pathway enrichment (GO and KEGG) and GSVA analyses, were performed across individual animal replicates (n=3 per species). Gene Ontology (GO) and Kyoto Encyclopedia of Genes and Genomes (KEGG) enrichment analyses of DEGs were performed based on the hypergeometric distribution test. Gene Set Variation Analysis (GSVA) converted the expression matrix into pathway enrichment score matrices, and pathways with significant differences were analyzed using the limma package.

SCENIC transcription factor identification and target gene enrichment analysis

Given that the function of cell types is maintained through the coordinated interactions of transcription factors (TFs) and their corresponding target genes, to identify active TFs in different subtypes of the lungs of yak, dzho and cattle, we conducted single-cell TF network inference analysis using pySCENIC, followed by KEGG analyses of TFs enriched in yak in each subtype.

uncorrected proof

Pseudotime analysis

Dynamic changes in the developmental processes of $CD4^+$ T cells and fibroblasts were constructed respectively based on the Monocle2 package. The 'plot cell trajectory' function was employed to draw pseudotime trajectory plots for different cell types, whereas the 'plot pseudotime heatmap' function was used to generate heatmaps of highly variable genes.

Cell communication analysis

Using CellPhoneDB (version 2.0) to identify ligand–receptor pairs in scRNA-seq data based on default parameters, we focused only on those receptors and corresponding ligands that were expressed in at least 10% of the cell populations tested, which served as a valid threshold for inferring the presence of interactions between different cell types. The complex network of ligand–receptor interactions and their intensity differences among cell subtypes were visualised using 'circlize' and 'ggplot2'.

PPI network construction

The Search Tool for the Retrieval of Interacting Genes (STRING) is an online tool that assesses protein–protein interaction (PPI) network information. STRING (version 11.0) was used to evaluate the potential PPI relationships among those DEGs.

Fluorescence RNA in situ hybridisation

To achieve in situ detection of specific targets within lung tissue, we fixed the collected lung tissue samples with 4% paraformaldehyde and embedded them in paraffin to prepare 6 μm-thick sections. Fluorescence in situ hybridisation to detect corresponding targets was performed according to the ViewRNA™ Tissue Fluorescence Assay kit (Invitrogen, #QVT0700) instructions. In the experiment, probes for multiple specific targets were hybridised at a dilution of 1:40 under 40 °C for 2 h. Label Probes (Alexa Fluor™ 647, Alexa Fluor™ 546 and Alexa Fluor™ 488) were used at a dilution of 1:25. Finally, sections

Uncorrected proof

were counterstained with DAPI and mounted using ProLong Gold Antifade Mountant (Invitrogen, #P36930). Fluorescence images were captured using a laser scanning confocal fluorescence microscope (ZEISS, LSM900).

The following specific target probes were used in the study: FMO1 (Invitrogen, #VF6-4030788), GREM1 (Invitrogen, #VF1-4037770), C2 (Invitrogen, #VF6-4041029), COL1A2 (Invitrogen, #VF4-4028128), ATF7IP (Invitrogen, #VF6-4034013-VC), GIMAP4 (Invitrogen, #VF6-4031593-VC), CD28 (Invitrogen, #VF6-4027337-VT), CD4 (Invitrogen, #VF4-4028887-VC), RHOQ (Invitrogen, #VF6-4035408-VT), ADGRG1 (Invitrogen, #VF6-4031124-VT) and CD8A (Invitrogen, #VF1-4027346-VT). In addition, a positive control probe GAPDH (Invitrogen, #VF1-11674) was used to validate the experimental system.

Immunohistochemistry

As previously described, 6 μm-thick lung paraffin sections were prepared. We initially baked the sections at 60 °C for 1 h, followed by xylene deparaffinisation and graded hydration (100%, 95%, 70% and 50% ethanol). Antigen retrieval was then conducted through high-pressure heating in 10 mM pH 6.0 citrate–citrate sodium buffer, endogenous peroxidase was inactivated with 3% H_2O_2, perforation was achieved with 0.1% Triton X-100 and blocking was performed at room temperature with 3% BSA in PBS. Subsequently, sections were incubated overnight at 4 °C with primary antibodies specific to a range of target antigens, followed by color development with horseradish peroxidase (HRP)-conjugated secondary antibodies, haematoxylin re-staining, hydration (1% HCl in 75% ethanol), dehydration (95% and 100% ethanol) and mounting with neutral balsam. Finally, images were captured using an automatic digital slide scanner (KFBIO). Image-Pro Plus version 6.0 software was used to assess the area and density of the dyed region, and the mean optical density (MOD) value of the lHC section.

Uncorrected proof

The following specific target antigens were used in the study: GREM1 (rabbit, Abcam, #ab22138, 5 μg/mL), FMO1 (rabbit, Invitrogen, #PA5-54865, 1:350), C2 (rabbit, Invitrogen, #PA5-122183, 10 μg/mL), GIMAP4 (rabbit, Bio-Techne, #NBP1-83777, 1:250), MCAF (rabbit, Bethyl, #IHC-00187-T, 1:100), CD28 (rabbit, Abcam, #ab203084, 1:200), RHOQ (rabbit, Invitrogen, #MA5-37999, 1:100) and ADGRG1 (rabbit, Invitrogen, #720373, 2 μg/mL).

Western Blot

Lung tissues were homogenized in RIPA buffer (Sigma Aldrich, #R0278) and centrifuged at 13000×g for 5 min. Supernatants were collected and total protein levels were measured using BCA protein assay (Thermo Scientific, #A65453). Proteins were separated by SDS-PAGE and transferred to polyvinylidene fluoride membranes (Millipore, #IPVH00010). After overnight incubation with primary antibodies, bands were washed three times with TPBS containing 0.05% Tween-20 and incubated with horseradish peroxidase (HRP)-conjugated secondary antibody (goat anti-rabbit, Abcam, #ab6702, 1:5000) for 1 h at room temperature. Signals were visualized with enhanced chemiluminescence (Bio-Rad, #1705060) and imaged using an iBright CL1000 imaging system (Invitrogen, A32747) after an additional wash. Image-Pro Plus version 6.0 software was used to assess the grayscale values of the bands.

The following specific primary antibodies were used in the study: NF-κB p65 (rabbit, Cell Signaling Technology, #8242, 1:1000), Phospho-NF-κB p65 (Ser536) (rabbit, Cell Signaling Technology, #3033, 1:1000), Akt (rabbit, Cell Signaling Technology, #4691, 1:1000), Phospho-Akt (Ser473) (rabbit, Cell Signaling Technology, #4060, 1:2000), FAK (rabbit, Cell Signaling Technology, #3285, 1:1000), Phospho-FAK (Tyr397) (rabbit, Cell Signaling Technology, #3283, 1:1000) and β-Actin (rabbit, Cell Signaling Technology, #8457, 1:1000).

Uncorrected proof

Quantitative reverse transcription PCR

Total RNA was extracted from lung tissues of yak dzho and cattle, and Nanodrop (Thermo, NanoDrop One C) was used to detect the concentration and purity of total RNA. PrimeScript RT Reagent Kit with gDNA Eraser (Takara, #RR047A) was used for cDNA synthesis. Quantification of target genes was performed by real-time fluorescence quantitative PCR using TB Green Premix Ex Taq II (Takara, #RR820A), with β-actin as an internal reference. The relative expression levels of the target genes in different samples were calculated based on the $2^{-\Delta\Delta Ct}$ method. All statistical analyses of the data were carried out using GraphPad Prism software version 9.5, and one-way ANOVA with Tukey's multiple comparisons test was used for analysis.

Fluorescence-activated cell sorting

Lung lobes were collected immediately after yak slaughter, rinsed with HBSS and immersed in Tissue Storage Solution (Miltenyi Biotec, #130-100-008). The tissues were then trimmed, minced and dissociated in gentleMACS™ C Tubes (Miltenyi Biotec, #130-093-237) using the gentleMACS™ Dissociator (program m_lung_01, then m_lung_02) with a lung dissociation kit enzyme mix (Miltenyi Biotec, #130-095-927). The suspension was then filtered through 70 μm and 40 μm strainers, RBC-lysed and counted to obtain single-cell suspensions.

For CD4 *ATF7IP*$^{+}$-enriched population sorting, because the core subtype marker ATF7IP is an intracellular nuclear protein unsuitable for live-cell isolation, CD127 was selected as a surrogate surface marker based on scRNA-seq analysis showing its highest specificity and expression enrichment in this cluster. Cells were pre-enriched using a mouse CD4^{+} T cell isolation kit (Biosharp, #BL1268B) according to the manufacturer's instructions. 10^{6}–10^{7} cells were incubated with Zombie Violet™ (BioLegend, #423113, 1:1000/10^{6} cells), washed with FACS buffer and stained on ice with an antibody panel: CD45^{+} (clone

Uncorrected proof

30−F11, Proteintech, #PE-65087, 2.5 μL/10^6 cells), $CD3^+$ (clone 17A2, BioLegend, #100220, 1.25 μL/10^6 cells), $CD4^+$ (clone GK1.5, Proteintech, #FITC-65104, 1 μL/10^6 cells) and $CD127^+$ (clone A7R34, Proteintech, #CL647-65093, 1 μL/10^6 cells). Cells were resuspended at 10^6 cells/500 μL for sorting.

For gCap-enriched population sorting, dissociated cells were plated on TC-treated dishes pre-coated with 0.1% gelatin. Differential adhesion was used to remove fibroblasts. Non-adherent cells were transferred to gelatin-coated plates and cultured in ECM endothelial medium (ScienCell, #1001). After 48 h non-adherent cells were discarded. When the cells reached 60−70% confluence, they were detached using TrypLE™ Express (Invitrogen, #12604013), prepared as single-cell suspensions and incubated with Zombie Violet. They were then stained with the gCap panel: $CD45^-$ (clone 30−F11, Proteintech, #PE-65087, 2.5 μL/10^6 cells), $CD31^+$ (clone 390, Proteintech, #FITC-65058, 1 μL/10^6 cells) and $CD144^+$ (clone BV13, Biolegend, #138011, 0.3 μL/10^6 cells). The cells were then resuspended at a concentration of 10^6 cells/500 μL for sorting.

Activation of CD4 *ATF7IP*$^+$-enriched population

Non-TC-treated 24-well plates were washed twice with HBSS, followed by the addition of anti-CD3 antibody (Biolegend, #100339, 3 μg/mL) and incubation at 37 °C for 2 h. After removing the unbound antibody, wells were washed twice with HBSS and kept for subsequent use. The sorted CD4 *ATF7IP*$^+$-enriched population was then expanded in T-cell expansion medium: 87% RPMI 1640, 10% FBS, 100 U/mL penicillin–streptomycin, 4 mM GlutaMAX™, 100 μg/mL mycoplasma removal reagent, 3 μg/mL anti-CD28 (Biolegend, #102115) and 10 ng/mL hIL-2 (MCE, #HY-P7037).

Immunofluorescence

The expanded CD4 *ATF7IP*$^+$-enriched population was fixed in 4% PFA for 15 min, washed with PBS and permeabilised for 10 min. Following PBST washing, cells were blocked with QuickBlock™ buffer (Beyotime, #P0260) for 30 min, then incubated overnight at 4 °C with anti-ATF7IP primary antibody

Uncorrected proof

(Proteintech, #14699-1-AP; 1:500). After further PBST washes, cells were stained with goat anti-rabbit IgG secondary antibody (Proteintech, #SA00013-2, 1:500) for 2 h at RT, stained with DAPI, washed again and dropped onto adhesive slides. After air-drying in the dark, slides were mounted with ProLong Gold Antifade Mountant and imaged under a laser scanning confocal fluorescence microscope.

The sorted gCap-enriched population was seeded onto round coverslips in 6-well plates and cultured for 48 h, then fixed with 4% PFA. Subsequent staining procedures were performed using anti-APJ antibody (Proteintech, #20341-1-AP; 1:500) following the same protocol as above.

Establishment and validation of hypoxia model

To simulate chemical hypoxic conditions, sorted yak CD4 *ATF7IP*$^{+}$-enriched and gCap-enriched populations were treated with 200 μmol/L $CoCl_2$ (Sigma Aldrich, #15862-1ML-F) (Lin et al., 2015). Chemical hypoxia induced by $CoCl_2$ was selected to establish a highly controllable system for sustained HIF-1α stabilization while avoiding reoxygenation stress associated with frequent ambient oxygen exposure during multi-step treatments. The expression levels of HIF-1α (rabbit, Cell Signaling Technology, #36169, 1:1000) in both cell types were assessed by RT-qPCR and Western blot to evaluate the efficiency of chemical hypoxia induction. Detailed procedures for RT-qPCR and Western blot are described in Sections “Western Blot” and “Quantitative reverse transcription PCR”.

Transwell co-culture of yak CD4 *ATF7IP*$^{+}$-enriched and gCap-enriched populations

To investigate whether the CD4 *ATF7IP*$^{+}$-enriched population could alleviate hypoxia-induced dysfunction in the gCap-enriched population, an indirect co-culture system was established using 6-well Transwell inserts (pore size 0.4 μm), which enabled non-contact co-culture between these two enriched populations. The gCap-enriched population was seeded into the lower chamber of Transwell inserts at a density of 2.5×10^5 cells/mL in ECM endothelial medium (2.6 mL per well). The CD4 *ATF7IP*$^{+}$-enriched

Zoological Research

population was expanded for 48 h and then seeded into the upper chamber at a concentration of 5×10^5 cells/mL (1.5 mL per insert) using T-cell basic medium: 87% RPMI 1640, 10% FBS, 100 U/mL penicillin–streptomycin, 4 mM GlutaMAX™ and 100 μg/mL mycoplasma removal reagent. These specific seeding densities and cell ratios were optimized through preliminary experiments to achieve an optimal monolayer confluence for gCap cells while maintaining cell viability and robust paracrine signaling during co-culture.

DIA proteomic analysis

Based on the CCK-8 assay results, we identified 24 h as the optimal time point, at which cellular lysates were collected for DIA-based cellular proteomic analysis. All proteomic experiments were performed with three independent biological replicates per group (n=3). CD4 *ATF7IP*$^+$ proteomic groups included: (1) CD4 *ATF7IP*$^+$-enriched population under normoxia: T_NC_P (normal condition); (2) CD4 *ATF7IP*$^+$-enriched population under hypoxia: T_HC_P (hypoxic condition); (3) CD4 *ATF7IP*$^+$-enriched population co-cultured with the gCap-enriched population under hypoxia: T_HCC_P (hypoxic co-culture). gCap proteomic groups included: (1) gCap-enriched population under hypoxia: EC_HC_P (hypoxic condition); (2) gCap-enriched population co-cultured with the CD4 *ATF7IP*$^+$-enriched population under hypoxia: EC_HCC_P (hypoxic co-culture).

Spectronaut 19 software was used for database searching and quantitative analysis. The reference database was UniProt *Bos mutus grunniens* (Taxon ID: 30521). The main search parameters were as follows: peptide length 7−52 aa; enzyme specificity trypsin/P; maximum missed cleavages 2; variable modifications included oxidation (M) and acetylation (Protein N-term); fixed modification carbamidomethyl (C); Protein FDR<=0.01; Peptide FDR<=0.01; Peptide Confidence>=99%; XIC width<=75 ppm. Protein quantification was performed using the MaxLFQ algorithm, and raw protein intensity data were normalized using the median normalization approach across samples. Differentially expressed proteins (DEPs) were identified

Uncorrected proof

using the t.test functionn in R with thresholds of $P<0.05$ and FC>1.2, and multiple testing corrections were performed using the Benjamini-Hochberg method to control the false discovery rate (FDR<0.05). Functional annotation and pathway enrichment analysis of DEPs were conducted using the GO and KEGG databases, respectively.

Optimal concentration of GPI/AMF cytokine

The gCap-enriched population cultured under standard conditions was treated with recombinant GPI/AMF protein (MCE, #HY-P71680) at concentrations of 0, 0.1, 0.2, 0.4, 0.6, 0.8, 1 and 1.5 μg/mL for 24 h (Araki et al., 2009; Lin et al., 2015). Cell viability was assessed using the CCK-8 assay after treatment to evaluate gCap activity. The optimal concentration of recombinant GPI/AMF for subsequent experiments was determined based on the dose−response results.

Construction of recombinant adenoviral vector and transduction of the CD4 *ATF7IP*$^{+}$-enriched population

Recombinant adenoviruses harboring a short hairpin RNA (shRNA) targeting the GPI gene (ADV1-GPI-Bos) and a negative control virus (ADV1-NC) were constructed by GenePharma (Shanghai, China). These vectors feature a U6 promoter driving shRNA expression and a CMV-driven GFP reporter. The specific interference target sequence for *GPI* was 5'-CCCAGTGACTTCTCACGATTC-3', whereas the negative control sequence was 5'-TTCTCCGAACGTGTCACGT-3'. Briefly, the shRNA-encoding shuttle vector and the E1/E3-deleted Ad5 backbone plasmid were co-transfected into 293A packaging cells using the RNAi-Mate (GenePharma, #G04001) transfection reagent. The transfected cells were maintained until the appearance of a visible cytopathic effect (CPE) and the formation of viral plaques, indicating successful viral replication. Viral particles were released from the cells via three cycles of freezing and thawing, followed

Uncorrected proof

by purification using CsCl density gradient centrifugation to ensure high purity. The viral titer was determined to be 1×10^8 PFU/mL via end-point dilution assay by monitoring CPE in 293A cells.

The CD4 *ATF7IP*$^+$-enriched population was isolated and activated using anti-CD3 and anti-CD28 antibodies (as detailed in Section "Activation of CD4 *ATF7IP*$^+$-enriched population"). At 12 h post-activation, the cells were transduced with the recombinant adenovirus at a multiplicity of infection (MOI) of 100 PFU/cell in the presence of 5 μg/mL Polybrene to enhance infection efficiency. The cells were incubated with the recombinant adenovirus for 24 h, followed by a wash step to remove free viral particles. At 48 h post-transduction, the knockdown efficiency of GPI/AMF was validated by RT-qPCR (primer listed in Supplemental Table S5; see Section "Quantitative reverse transcription PCR"). Prior to subsequent co-culture assays, the transduced cells were washed three times with PBS to ensure the complete removal of residual virus and prevent non-specific effects on the gCap-enriched population.

Secretion and functional validation of the GPI/AMF cytokine

Five experimental groups were established as follows: (1) gCap-enriched population treated with recombinant GPI/AMF protein under hypoxic conditions (Hyp + EC + AMF); (2) gCap-enriched population under hypoxic conditions (Hyp + EC); (3) CD4 *ATF7IP*$^+$-enriched population under hypoxic conditions (Hyp + T); (4) gCap-enriched population co-cultured with the CD4 *ATF7IP*$^+$-enriched population under hypoxic conditions (Hyp + T/EC); (5) CD4 *ATF7IP*$^+$-enriched population with adenoviral *GPI* interference co-cultured with the gCap-enriched population under hypoxic conditions (Hyp + T/EC + Ad-shGPI). All treatments across these groups were conducted for 24 h.

Groups (3) and (4) were compared to assess GPI/AMF expression under hypoxic and co-culture conditions. GPI/AMF protein levels were measured in both the intracellular fraction and the culture supernatant of the

Uncorrected proof

CD4 *ATF7IP*$^{+}$-enriched population using an ELISA kit (Finetest, #EH3165). Meanwhile, intracellular GPI/AMF mRNA levels were quantified by RT-qPCR.

To further evaluate the regulatory role of GPI/AMF in the gCap-enriched population, groups (1), (2), (4) and (5) were compared. The cell viability of the gCap-enriched population was assessed using the CCK-8 assay, while oxidative stress levels were determined through ROS detection.

AMFR Receptor-Blocking Assay

To investigate whether the AMF cytokine exerts its protective effects via the AMFR/gp78 receptor, a receptor-blocking assay was conducted. The gCap-enriched population was pre-incubated with a functional neutralizing anti-AMFR antibody (clone 3F3A, Sigma-Aldrich, #MABC949) prior to AMF treatment (Nabi et al., 1990). The subsequent impact of AMFR blockade on cell viability and ROS levels was evaluated using CCK-8 and ROS detection assays, respectively, to determine the functional necessity of the AMF-AMFR interaction for gCap hypoxic adaptation.

Statistical analysis

All values were expressed as mean ± standard error (SEM). All *in vitro* functional assays were performed using primary cells isolated from a single yak donor; thus, the reported "n=3" represents three independent experimental replicates from this same primary-cell source, with each sample measured in technical triplicates. Differences between groups were analyzed using one-way analysis of variance (ANOVA), followed by post hoc Tukey's multiple comparisons test, and the results were considered statistically significant at $P<0.05$. Different uppercase and lowercase letters between groups indicate $P<0.01$ and $P<0.05$, respectively.

uncorrected proof

RESULTS

Construction of single-cell transcriptomic atlas of lung in yak, dzho and cattle

By constructing lung single-cell transcriptomes of yak, dzho and cattle via scRNA-seq, a total bovine lung single-cell transcriptome encompassing 67,984 cells was generated after strict quality control (Figure 1A; Supplemental Table S1). Clustering of cells based on the expression profiles yielded 17 cell clusters (Supplemental Figure S1B), corresponding to six major cell types: T&NK cells (41.35%, *CD3E*), fibroblasts (9.68%, *PDGFRB*), myeloid cells (20.42%, *CLEC4A*), B&plasma cells (8.49%, *CD79B*), endothelial cells (13.14%, *MYCT1*) and epithelial cells (6.92%, *MUC1*; Figure 1B; Supplemental Figure S1D−F, H and I). The identities of these cell types were confirmed by the expression of specific marker genes (Figure 1C; Supplemental Figure S2). While the major cell types were conserved across species, their proportions varied significantly (Supplemental Figure S1C, G and J). T&NK cells were the predominant cell type, exhibiting a distinct descending trend in abundance from yak to dzho to cattle (Supplemental Table S2).

A total of 51 different cell subtypes were identified using known and newly defined marker genes (Supplemental Table S3), containing 24 T&NK subtypes (including 10 newly identified subtypes), 8 fibroblast subtypes (including 3 newly identified subtypes), 5 endothelial subtypes, 4 myeloid subtypes, 4 B&Plasma subtypes and 6 epithelial subtypes, resulting in a complete single-cell transcriptomic atlas (Figure 2B) of the lungs of yak (Figure 2C), dzho (Figure 2D) and cattle (Figure 2E). Here, these newly identified subtypes are defined as cell clusters with distinct marker expression signatures that have not been previously described in published bovine or mammalian lung single-cell atlases. The bar graph (Figure 2A; Supplemental Figure S3A) shows the differences in the proportion of cell numbers of all subtypes among yak, dzho and cattle. Among the 24 identified T&NK cell subtypes, the cell numbers of 6 subtypes

Uncorrected proof

403 demonstrated differences (P<0.05) across the yak, dzho and cattle groups (Supplemental Figure S4;
404 Supplemental Table S4).

405 **Cellular heterogeneity of T&NK, fibroblasts, myeloid, B&Plasma, endothelial and epithelial cells in**
406 **yak, dzho and cattle**

407 **T&NK cells:** T&NK cells were clustered into 15 clusters (Supplemental Figure S5A), and based on their
408 expression profiles, we initially identified 6 cell subtypes (Supplemental Figure S5B), including $CD4^+$ T
409 cells, $CD8^+$ T cells, NK cells, NKT cells, ILCs and cycling T cells. Next, we further performed
410 dimensionality reduction and clustering on the $CD4^+$ T cell (Supplemental Figure S5C) and $CD8^+$ T cell
411 (Supplemental Figure S5E) subtypes, followed by cell annotation (Supplemental Figure S5D and F). In total,
412 we identified 24 T&NK cell subtypes with distinct expression profiles, including CD4 *ATF7IP*$^+$ (6.57%,
413 *CAMK4*), CD4 Exhausted (2.91%, *CTLA4*), CD4 Th1 like (9.15%, *PYGO1*), CD4 *GIMAP4*$^+$ (3.94%,
414 *GIMAP4*), CD8 *BCL2L11*$^+$ (1.32%, *RHOQ*), CD8 *KLRD1*$^+$ (1.00%, *KLRD1*), CD8 Naive (11.69%, *TRGC3*),
415 and CD8 *TRGC6*$^+$ (2.38%, *TRGC6*; Figure 3A; Supplemental Table S3). The most representative marker
416 genes for each subtype, based on their expression levels, were overlaid on the UMAP plot (Supplemental
417 Figure S5G). A bubble plot (Supplemental Figure S6) displayed the top marker genes for all subtypes, and
418 a bar graph (Supplemental Figure S3B; Supplemental Figure S5H) showed the differences in cell number
419 proportions among yak, dzho and cattle for the 24 T&NK cell subtypes. Notably, the CD4 *ATF7IP*$^+$ subtype,
420 which represented the largest novel subtype, exhibited a marked reduction in abundance from yak to dzho
421 to cattle (Figure 3D; Supplemental Table S4).

422 **Fibroblasts:** Fibroblast were clustered into 10 clusters (Supplemental Figure S14A), from which we
423 identified 8 cell subtypes of fibroblasts with distinct expression profiles, namely, Fibromyo./SMCs (7.86%,
424 *ADGRL3*), Pericytes (4.33%, *RGS5*), Fib *Col13a1*$^+$ (20.03%, *COL3A1*), AdvF (8.95%, *CHI3L1*), Fib *NOG*$^+$

Uncorrected proof

(23.96%, *GREM1*), Fib *RYR2*$^+$ (14.85%, *RYR2*), Fib *C2*$^+$ (13.78%, *C2*) and Fib *S100G*$^+$ (6.23%, *S100G*; Supplemental Figure S13A; Supplemental Table S3). The Fibromyo./SMC cluster expresses a mixture of fibroblasts, myofibroblasts and smooth muscle cells (Hurskainen et al., 2021), which correspond in part to the fibromyocyte described by Travaglini et al. (Travaglini et al., 2020). Fib *Col13a1*$^+$ expresses additional *Col13a1* fibroblast marker and multiple pan-fibroblast markers (Hurskainen et al., 2021). Fib *S100G*$^+$ highly expresses *S100G* and *PI16* genes, and it functions similarly to adventitial stromal cells (Buechler et al., 2021). Subtype identities were validated by the expression of specific marker genes (Supplemental Figure S14F, Supplemental Figure S15). Among the three newly identified subtypes, Fib *NOG*$^+$ was predominantly found in cattle, whereas Fib *RYR2*$^+$ and Fib *C2*$^+$ were markedly enriched in yak and dzho (Supplemental Figure S3C; Supplemental Figure S13D; Supplemental Figure S14D; Supplemental Table S4).

Myeloid: Myeloid cells were clustered into 13 clusters (Supplemental Figure S21A), from which we identified 4 subtypes of myeloid cells with unique expression profiles, namely, macrophages (63.78%, *C1QB*), monocytes (17.45%, *OSM*), neutrophils (13.62%, *CDA*) and dendritic cells (5.14%, *CLEC9A*; Supplemental Figure S21B; Supplemental Table S3). These annotations were validated via the expression of specific marker genes, and their relative abundances were quantified across yak, dzho, and cattle (Supplemental Figure S21C, E). Neutrophils were almost entirely distributed in yak (Supplemental Figure S21D, F).

B&Plasma cells: B&Plasma cell were clustered into 8 clusters (Supplemental Figure S23A), from which we identified 4 subtypes of B&Plasma cells with distinct expression profiles, namely, mature B cells (76.09%, *RIN3*), Immature B Cells (5.30%, *LY6D*), Plasma Cells (8.79%, *TNFRSF17*) and pro B cells (9.82%, *VPREB3*; Supplemental Figure S23B; Supplemental Table S3). Following validation via marker

Uncorrected proof

446 gene expression (Supplemental Figure S23C, E), we observed that Mature B and Pro B cells were
447 predominantly enriched in yak and dzho (Supplemental Figure S23D, F).

448 **Endothelial cells:** Endothelial cells were clustered into 10 clusters (Supplemental Figure S25A), and we
449 identified 5 subtypes of endothelial cells with distinct expression profiles, namely, aCap (20.05%, *EDNRB*),
450 gCap (18.14%, *CYP1A1*), artery (30.49%, *NTRK2*), vein (9.31%, *ACKR1*) and lymph (22.01%, *PROX1*;
451 Supplemental Figure S25B; Supplemental Table S3). Subtype identities were validated by marker expression
452 (Supplemental Figure S25D, F). Based on the classification by Gillich et al. (Gillich et al., 2020), we resolved
453 capillary endothelial cells into two functional subtypes: aCap (specialized for gas exchange) and gCap
454 (functioning as progenitors in homeostasis and repair). In our study, the gCap subtype was preferentially
455 enriched in yak and dzho, while cattle lungs were dominated by the aCap subtype (Supplemental Figure
456 S25C, E; Supplemental Table S4).

457 **Epithelial cells:** Epithelial cells were clustered into 11 clusters (Supplemental Figure S27A), and we
458 identified 6 epithelial cell subtypes with distinct expression profiles, namely, AT1 (35.56%, *AKAP2*), AT2
459 (36.18%, *HHIP*), basal (6.00%, *TP63*), ciliated (6.89%, *FAM81B*), club (14.37%, *FER1L6*) and tuft (1.00%,
460 *CA7*; Supplemental Figure S27B; Supplemental Table S3). Subtype identities were validated by marker
461 expression (Supplemental Figure S27D, F). The cell numbers of all subtypes were higher in cattle but lower
462 in yak and dzho (Supplemental Figure S27C, E).

463 **Identification and validation of newly species-specific subtypes in yak, dzho and cattle**

464 This study identified 10 new T&NK subtypes and 3 new fibroblast subtypes in bovine species. Among
465 the 10 bovine-specific T&NK cell subtypes (marked in blue in Supplemental Table S4), the CD4 *ATF7IP*$^{+}$,
466 CD4 Th1 like, CD8 *BCL2L11*$^{+}$ and CD8 *TRGC6*$^{+}$ subtypes were almost exclusively found in yak and dzho.
467 whereas the CD4 *GIMAP4*$^{+}$ subtype was predominantly found in cattle (Supplemental Table S4). Consistent

Uncorrected proof

with these cellular proportions, the expression profiles of their corresponding marker genes (*ATF7IP* for CD4 *ATF7IP*$^+$, *GIMAP4* for CD4 *GIMAP4*$^+$, *RHOQ* for CD8 *BCL2L11*$^+$, *ADGRG1* for CD8 *TRGC6*$^+$, and *CD28* for CD4 Th1 like) displayed matching species-specific divergence (Figure 3C). We experimentally validated the existence and spatial distribution of these five representative subtypes at both RNA and protein levels using fluorescence in situ hybridization (Figure 3E; Supplemental Figure S7A; Supplemental Figure S8A; Supplemental Figure S9A; Supplemental Figure S10A; and Supplemental Figure S20E) and immunohistochemistry (Figure 3F; Supplemental Figure S7B; Supplemental Figure S8B; Supplemental Figure S9B; Supplemental Figure S10B; Supplemental Figure S20C and D). Furthermore, given the high abundance of T&NK cells in lung tissue, tissue-level RT-qPCR analysis corroborated the scRNA-seq findings (primers listed in Supplemental Table S5, top 10 marker genes listed in Supplemental Table S6). The expression trends of representative marker genes were highly consistent with the bioinformatics data. Specifically, markers for the CD4 *ATF7IP*$^+$, CD4 Th1 like, CD8 *BCL2L11*$^+$ and CD8 *TRGC6*$^+$ subtypes were upregulated in yak and dzho, in contrast to the CD4 *GIMAP4*$^+$ marker, which was enriched in cattle (Supplemental Figure S5I).

Fib *NOG*$^+$, Fib *RYR2*$^+$ and Fib *C2*$^+$ were 3 new fibroblast subtypes identified in bovine species in this study (highlighted in green in Supplemental Table S4). Specifically, the Fib *RYR2*$^+$ and Fib *C2*$^+$ subtypes were almost exclusively found in yak and dzho, in contrast to the Fib *NOG*$^+$ subtype, which was predominantly observed in cattle (Supplemental Table S4). Consistent with the cellular abundance differences, the expression profiles of representative marker genes (*GREM1* for Fib *NOG*$^+$, *FMO1* for Fib *RYR2*$^+$, and *C2* for Fib *C2*$^+$) displayed matching species-specific variations (Supplemental Figure S13C). Subsequent experimental validation confirmed the existence and spatial distribution of these subtypes at both RNA and protein levels using FISH (Supplemental Figure S13E; Supplemental Figure S16A; Supplemental

Uncorrected proof

Figure S17A; and Supplemental Figure S20E) and IHC (Supplemental Figure S13F; Supplemental Figure S16B; Supplemental Figure S17B; Supplemental Figure S20C, D). Additionally, tissue-level RT-qPCR analysis corroborated the scRNA-seq data (primers listed in Supplemental Table S5, top 10 marker genes listed in Supplemental Table S6), demonstrating that markers for the Fib *RYR2*$^{+}$ and Fib *C2*$^{+}$ subtypes were upregulated in yak and dzho, while the Fib *NOG*$^{+}$ marker showed an opposite trend (Supplemental Figure S14C). Collectively, these findings not only validated the existence of the novel T&NK and fibroblast subtypes at the gene and protein levels but also confirmed their quantitative trends among the yak, dzho and cattle.

Specific expression patterns of differential subtypes in yak, dzho and cattle

To further investigate the alterations in the transcription profiles among yak, dzho and cattle, we performed differential expression analysis at the cell subtype levels. Notably, given their abundance and heterogeneity across species, the T&NK cell type was a major focus of our study.

T&NK cell subtypes: We selected the four T&NK subtypes almost exclusively found in yak and dzho (CD4 *ATF7IP*$^{+}$, CD8 *BCL2L11*$^{+}$, CD8 *TRGC6*$^{+}$ and CD4 Th1 like) to investigate species-specific immune features. Among them, the CD4 *ATF7IP*$^{+}$ subtype was the most abundant and exhibited the most pronounced interspecies differences. GSVA enrichment analysis revealed that these subtypes were primarily enriched in pathways related to the metabolism of essential amino acids, thiamine, and glutathione in yak and dzho (Supplemental Figure S11A–C). We then performed a combined differential analysis of these four subtypes against the remaining T&NK subtypes. Functional enrichment analysis revealed a robust pro-inflammatory signature in these yak enriched subtypes. Specifically, both GO and KEGG enrichment analyses highlighted the activation of critical immune signaling cascades, including the I-kappaB kinase/NF-kappaB, T cell receptor (TCR) and C-type lectin receptor pathways, alongside enhanced cytokine production (interleukin-

Uncorrected proof

6 and IL-17 signaling) (Supplemental Figure S12A–B; Supplemental Table S7). To experimentally validate the activated signaling landscape, we first confirmed the upregulation of key pathway components. Both RT-qPCR and Western Blot analyses demonstrated that the expression of critical nodes within major immune signaling cascades, including the NF-kappaB and TCR signaling pathways, followed a consistent yak>dzho>cattle gradient (Supplemental Figure S12C; Supplemental Figure S20A, B; Supplemental Table S7). Seeking to identify the central regulators driving these pathways, we constructed a PPI network based on the top 20 upregulated and downregulated genes. Network analysis highlighted CD4 and NKG7 as central hub nodes with opposing expression patterns (Figure 3B; Supplemental Figure S11D). Subsequent RT-qPCR validation (for primers, see Supplemental Table S5) confirmed that *CD4* was markedly upregulated in yak (yak>dzho>cattle), whereas *NKG7* was enriched in cattle (P<0.01; Supplemental Figure S5J). These findings position *CD4* and *NKG7* as potential key mediators modulating multiple enhanced signaling cascades, including NF-kappaB and TCR, that characterize the yak specific subtypes.

Fibroblast subtypes: Within the fibroblast population, the yak specific Fib $RYR2^{+}$ and Fib $C2^{+}$ subtypes exhibited unique metabolic and signaling profiles. GSVA profiling revealed that these subtypes were characterized by the enrichment of glycerophospholipid metabolism and peroxisome processes in yak and dzho compared to cattle (Supplemental Figure S18). Functional analyses via GO and KEGG analyses linked these yak specific subtypes to critical high-altitude adaptive mechanisms, specifically glucose homeostasis and structural remodeling. Comparative analysis against other fibroblasts revealed a convergent enrichment of pathways governing energy metabolism, including glucose metabolic process, insulin, cAMP and PI3K-Akt signaling, as well as cell adhesion processes such as integrin binding and focal adhesion (Supplemental Figure S19A−B; Supplemental Table S8). Experimental verification via RT-qPCR and Western Blot confirmed the activation of these metabolic and adhesion pathways in yak and dzho (Supplemental Figure

Zoological Research

S19C; Supplemental Figure S20A, B; Supplemental Table S8). Subsequent PPI network analysis revealed *IGF2* and *MYL9* as the most connected hub genes (Supplemental Figure S13B; Supplemental Figure S14B). Validation via RT-qPCR highlighted their distinct regulatory profiles (for primers, see Supplemental Table S5), demonstrating that *IGF2* was markedly upregulated in yak, whereas *MYL9* was predominantly enriched in cattle (P<0.01; Supplemental Figure S14E). Mechanistically, these hub genes are implicated in modulating multiple signaling cascades, including the PI3K-Akt and focal adhesion signaling pathways.

Neutrophils subtype: As the only myeloid subtype preferentially enriched in yak, neutrophils were prioritized for interspecies comparative analysis. GSVA results revealed that yak and dzho neutrophils were characterized by active biosynthesis of essential amino acids and glutathione metabolism relative to cattle (Supplemental Figure S22C). Functionally, GO and KEGG enrichment analyses highlighted a pronounced pro-inflammatory state, characterized by the activation of critical immune signaling cascades, including the NF-kappaB, TNF, IL-17, Chemokine, and C-type lectin receptor pathways, alongside enhanced inflammatory responses (Supplemental Figure S22A−B).

Pro B subtype: Given its high abundance and preferential enrichment in yak, the Pro B subtype was selected for detailed interspecies comparison. GSVA results showed that yaks and dzhos exhibited heightened activity in amino acid metabolism, ECM−receptor interactions and RNA degradation pathways compared to cattle (Supplemental Figure S24C). Furthermore, GO and KEGG enrichment analyses uncovered a distinct regulatory network in yak that involved mRNA 3'-end processing and protein autophosphorylation, coupled with the activation of critical signaling cascades including the B cell receptor, C-type lectin receptor, IL-17 and glucagon signaling pathways (Supplemental Figure S24A−B).

gCap subtype: The gCap subtype was selected for interspecies comparison of endothelial cells, given their pivotal status as a progenitor population possessing self-renewal and differentiation capacities essential

Uncorrected proof

for replenishing exhausted endothelial pools and orchestrating vascular remodeling and homeostasis. In the interspecies comparison, yak and dzho gCap subtype displayed a unique profile of adaptive remodeling. Comparative GSVA analyses identified a specific metabolic signature in yak and dzho, dominated by glycerophospholipid and non-essential amino acid metabolism relative to cattle (Supplemental Figure S26C). Furthermore, GO and KEGG enrichment analyses highlighted a distinct functional landscape of vascular remodeling and structural integrity, featuring the PI3K/Akt pathway, growth factor receptor signaling pathway, cell migration and reactive oxygen species metabolism alongside structural mechanisms including cell adhesion and adherens junctions (Supplemental Figure S26A−B).

Species-specific TFs regulatory networks in the T&NK subtype

Transcription factors (TFs) serve as master regulators of gene expression and exhibit marked species specificity. In our single-cell atlas, the T&NK cells constituted the most abundant population, characterized by a marked predominance in yaks. Consequently, we applied single-cell regulatory network inference and clustering (SCENIC) analysis to the four yak enriched subtypes, namely CD4 *ATF7IP*$^{+}$, CD4 Th1 like, CD8 *BCL2L11*$^{+}$ and CD8 *TRGC6*$^{+}$, which collectively constitute the core immune populations in yak. Analysis of the regulatory network uncovered a distinct regulatory landscape driven by key lineage-specific transcription factors. Specifically, the CD4 *ATF7IP*$^{+}$ subtype was characterized by the high activity of Yy1, Rel and Zbtb37 (Supplemental Figure S28A), while the CD4 Th1 like subtype was dominated by Fli1 and Zbtb37 (Supplemental Figure S29A). In parallel, the CD8 *BCL2L11*$^{+}$ subtype showed strong enrichment for Bptf, Tbl1xr1 and Etv3 (Supplemental Figure S30A), whereas the CD8 *TRGC6*$^{+}$ subtype was primarily regulated by Foxo3, Atf4 and Etv3 (Supplemental Figure S31A). Functionally, these identified master regulators are pivotal in orchestrating inflammatory responses, immune activation and the maintenance of cellular homeostasis under stress. Notably, the identification of Rel as a key NF-kappaB subunit and Foxo3

Uncorrected proof

as a critical stress-response regulator offers a mechanistic explanation for the enhanced inflammatory profile and high-altitude adaptation observed in yak.

Further functional annotation of the target genes via KEGG analysis substantiated our findings, confirming that these regulons are responsible for activating critical immune signaling cascades, including the T cell receptor and C-type lectin receptor pathways (Supplemental Figure S28B; Supplemental Figure S29B; Supplemental Figure S30B; Supplemental Figure S31B). In summary, these data reveal a comprehensive transcriptional network orchestrating the immune response and homeostatic regulation in yak specific T&NK subtypes.

Pseudotime analysis of CD4$^+$ T among yak, dzho and cattle

Given that the T&NK lineage exhibited the most profound interspecies heterogeneity in our atlas, we reconstructed developmental trajectories to determine whether these phenotypic differences stem from divergent cell fate decisions. Indeed, trajectory analysis uncovered a marked species-specific bifurcation in differentiation pathways (Figure 4C−E). We speculated that among the CD4$^+$ T subtypes, CD4$^+$ T cells of yak and dzho were more inclined to differentiate into CD4 *ATF7IP*$^+$ and CD4 Th1 like subtypes, while CD4$^+$ T cells of cattle were more inclined to differentiate into CD4 *GIMAP4*$^+$ and CD4 Memory subtypes (Figure 4F; Supplemental Figure S33). To visualize the transcriptional dynamics driving this lineage divergence, we employed a pseudotime-ordered heatmap to resolve distinct gene expression modules (Supplemental Figure S34A). Module 4 emerged as the critical driver, showing a progressive increase in expression that paralleled the developmental trajectory of the yak enriched subtypes. Functional annotation of this module via KEGG analysis highlighted the activation of the T cell receptor, C-type lectin receptor and MAPK signaling pathways (Supplemental Figure S34B). These results corroborate our earlier regulatory analysis, indicating

Zoological Research

599 that the distinct pro-inflammatory profile and signaling activation are intrinsically programmed into the
600 developmental trajectory of yak T&NK cells.

601 **Intercellular communications in the differential subtype of yak**

602 The hypoxic environment of the plateau exerts a profound influence on the cellular composition and
603 interaction landscape of the lung. To characterize the interactions among lung cell subtypes associated with
604 high-altitude adaptability, we selected 12 subtypes with a high percentage in yak and dzho but a low
605 percentage in cattle: Fib *RYR2*$^+$, Fib *C2*$^+$, CD4 *ATF7IP*$^+$, CD4 Exhausted, CD4 Th1 like, CD8 *BCL2L11*$^+$,
606 CD8 *KLRD1*$^+$, CD8 Naive, CD8 *TRGC6*$^+$, neutrophils, pro B and gCap. On the basis of the quantity of
607 receptor–ligand pairs, we constructed an intercellular communication network. The heatmap (Figure 4B)
608 illustrated the quantity of interaction pairs among different cell subtypes, with the majority of ligands being
609 produced by gCap, Fib *C2*$^+$ and neutrophils, corresponding to receptors in themselves (gCap, Fib *C2*$^+$ and
610 neutrophils) and in Fib *RYR2*$^+$. Additionally, gCap, Fib *C2*$^+$ and neutrophils produced a large number of
611 receptors corresponding to their own ligands and the ligands of the remaining CD4$^+$ T and CD8$^+$ T subtypes.

612 The bubble chart (Supplemental Figure S32) and the circos plot (Figure 4A) illustrated the interacting
613 receptor–ligand pairs among different subtypes. Neutrophils predominantly regulated other cell types
614 through their ligands Ccl4 and Tnfrsf1b by recognising corresponding receptors. gCap was primarily
615 recognised by the receptors through Tnfsf10 and Rps19, whereas Fib *C2*$^+$ mainly interacted with its receptors
616 through Igf2 and Rps19. Furthermore, the seven subtypes of CD4$^+$ T and CD8$^+$ T mainly regulated gCap,
617 Fib *C2*$^+$ and neutrophils by recognizing their respective receptors through the ligands of the Rps19, Ccl and
618 Tnf families. These interactions delineate a complex regulatory network of immune-structural crosstalk, in
619 which T cells orchestrate the inflammatory and angiogenic remodeling of the lung microenvironment.

uncorrected proof

Based on these network insights, we sought to identify the most critical interaction axis driving yak lung adaptation. Given that the T&NK cells constitute the largest proportion of the bovine lung immune landscape, the CD4 *ATF7IP*$^{+}$ subtype stood out as the most abundant and species-divergent population. Detailed analysis of receptor-ligand pairs revealed a remarkably high frequency of significant receptor-ligand interaction pairs between the CD4 *ATF7IP*$^{+}$ subtype and the gCap subtype (Supplemental Table S9). This finding highlights a pivotal signaling axis wherein the dominant immune population communicates directly with the core progenitor endothelial cells to maintain vascular homeostasis under hypoxia. Furthermore, from an evolutionary perspective, endothelial and immune cells share a common ancestral origin, which underscores their intimate functional coupling in establishing tissue-specific immune homeostasis. Therefore, the interaction between the CD4 *ATF7IP*$^{+}$ subtype and the gCap subtype represents a prioritized target for mechanistic study. Based on these findings, we designed co-culture experiments involving these two key subtypes to experimentally validate their interaction and further investigate the cellular mechanisms underlying high-altitude adaptation in the yak lung.

CD4 *ATF7IP*$^{+}$-enriched population regulates hypoxic adaptation of gCap-enriched population by secreting GPI/AMF

Using immunomagnetic bead sorting combined with fluorescence-activated cell sorting (FACS), we successfully isolated the yak lung CD4 *ATF7IP*$^{+}$-enriched (Zombie^{-}/CD45^{+}/CD3^{+}/CD4^{+}/CD127^{+}) and gCap-enriched (Zombie^{-}/CD45^{-}/CD31^{+}/CD144^{+}) populations (Figure 5A and D; Supplemental Figure S35C−D). Subsequent immunofluorescence staining supported the successful enrichment of the target CD4 *ATF7IP*$^{+}$ and gCap populations (Supplemental Figure S35A−B). The sorted cells were then exposed to 200 μmol/L $CoCl_2$ (Lin et al., 2015) for 48 h to induce chemical hypoxia. Detection of HIF-1α expression levels revealed

Zoological Research

markedly higher expression in the $CoCl_2$ treated group compared to the untreated control group, which fully validated the successful establishment of this chemical hypoxia model (Supplemental Figure S36C).

To elucidate the molecular mechanisms by which the CD4 *ATF7IP*$^+$-enriched population regulates the gCap-enriched population, we performed comparative proteomic analyses under 24 h (n=3 biological replicates; Supplemental Figure S36A−B) under hypoxic condition (HC) and hypoxic co-culture (HCC) conditions. The analysis revealed that co-culture triggered unique protein expression changes in both populations that were distinct from those caused by hypoxia alone (Supplemental Figure S37A−E; Supplemental Figure S38A−C). Bioinformatic analysis (GO and KEGG) of the differentially expressed proteins (DEPs) provided critical insight into the functional roles of each population within the co-culture environment. The CD4 *ATF7IP*$^+$-enriched population exhibited enrichment in pathways associated with its function as a secretory and immune regulator. Key enriched terms included complement and coagulation cascades, ECM-receptor interaction and hematopoietic cell lineage (Supplemental Figure S37F−I). In contrast, the gCap-enriched population showed a strong focus on pathways related to cell survival, adhesion and metabolic adaptation. Highly enriched terms involved crucial signaling hubs like the PI3K-Akt signaling pathway, mTOR signaling pathway and processes related to ROS regulation and adherens junctions (Supplemental Figure S38D−E).

To identify candidate proteins with potential secretory activity from the CD4 *ATF7IP*$^+$-enriched population that drive this regulation, we devised a stringent multi-step screening strategy. First, we focused on the CD4 *ATF7IP*$^+$-enriched population, targeting proteins that were specifically upregulated in the HCC group relative to the HC group, yet remained downregulated or undetectable in the HC group compared to the normal condition (NC) group. This analysis identified 173 interaction-dependent proteins enriched in 45 markedly altered KEGG pathways. Simultaneously, we analyzed the gCap-enriched population to identify

Uncorrected proof

663 the endothelial response to T cell signals. Out of 640 DEPs between the HCC and HC groups, we narrowed
664 the list to 94 annotated proteins that mapped to 22 differential pathways. Finally, we intersected these two
665 datasets to identify potential effectors. By excluding proteins that were downregulated in the gCap-enriched
666 population during co-culture, we successfully narrowed the candidates down to five cytokines (Supplemental
667 Table S10). Notably, the CD4 *ATF7IP*$^{+}$-enriched population exhibited minimal intracellular expression of
668 these candidate cytokines under hypoxia alone, whereas their protein levels were markedly upregulated upon
669 co-culture with the gCap-enriched population. This observation suggests an expression pattern that is not
670 autonomous but rather passively induced by intercellular crosstalk. Following the rigorous exclusion of non-
671 secretory proteins and those lacking secretory capacity in T cells, GPI/AMF emerged as the pivotal candidate
672 cytokine for subsequent functional validation of its actual extracellular secretion. Importantly, this proteomic
673 candidate is strongly corroborated by our single-cell cell–cell communication analysis. Within the scRNA-
674 seq dataset, the AMF (GPI)–AMFR ligand–receptor pair exhibited a statistically significant interaction score
675 between the CD4 *ATF7IP*$^{+}$ and gCap subtypes (interaction score=0.519, P=0.03). Furthermore, both the
676 ligand and receptor displayed robust, cell-type-specific expression in their respective target subtypes (ligand
677 expression level=2.92 in CD4 *ATF7IP*$^{+}$; receptor expression level=6.24 in gCap). These concordant
678 transcriptomic and proteomic findings jointly designate the GPI/AMF–AMFR axis as the key paracrine
679 mediator of CD4 *ATF7IP*$^{+}$–gCap crosstalk under hypoxia.

680 Next, we sought to determine the secretion dynamics of GPI/AMF by the CD4 *ATF7IP*$^{+}$-enriched
681 population under hypoxic conditions. ELISA analysis of the culture supernatant revealed a substantial
682 accumulation of AMF protein specifically in the co-culture system (Hyp + T/EC) compared to the CD4
683 *ATF7IP*$^{+}$-enriched population under hypoxic conditions (Hyp + T) (n=3 biological replicates; Figure 5C).
684 This protein-level finding was further corroborated by RT-qPCR, which demonstrated an upregulation of

Uncorrected proof

GPI mRNA within the CD4 *ATF7IP*$^{+}$-enriched population only under co-culture conditions with the gCap-enriched population (n=3 biological replicates; Figure 5B). Collectively, these results confirm that the CD4 *ATF7IP*$^{+}$-enriched population secretes GPI/AMF under hypoxic conditions and that this secretion is markedly amplified during co-culture. This validates our proteomic prediction that GPI/AMF secretion by the CD4 *ATF7IP*$^{+}$-enriched population is not autonomously induced, but represents a passive process stimulated by the gCap-enriched population.

GPI/AMF mediates hypoxic adaptation of the gCap-enriched population via PI3K/AKT signaling pathway

To investigate the regulatory effects of GPI/AMF on the gCap-enriched population, we established a dual experimental strategy involving exogenous protein supplementation and endogenous adenoviral interference. First, to determine the optimal concentration for exogenous treatment, we evaluated the proliferative response of gCap cells to a concentration gradient of recombinant GPI/AMF via a CCK-8 assay. The results indicated that GPI/AMF promoted proliferation in a concentration-dependent manner, achieving maximal efficacy at 0.2 μg/mL. Beyond this threshold (0.4−1.5 μg/mL), the proliferative effect reached saturation or exhibited a slight inhibitory trend (n=6 biological replicates; Figure 5E). Consequently, 0.2 μg/mL was selected as the optimal concentration for all subsequent experiments. In parallel, to block the endogenous source of the cytokine, we engineered a specific interference model in the CD4 *ATF7IP*$^{+}$-enriched population using a GPI-targeting recombinant adenovirus (Adv-shGPI-Bos) (Supplemental Figure S39B). Validation assays using RT-qPCR confirmed a significant suppression of both GPI/AMF mRNA transcription in the transduced CD4 *ATF7IP*$^{+}$-enriched population (n=3 biological replicates; Supplemental Figure S39A). This successfully confirmed the establishment of a GPI-interference model for subsequent co-culture experiments.

uncorrected proof

706 Building on these optimized models, we employed a positive/negative control strategy to definitively
707 dissect the rescue effect of the AMF cytokine. Functional analysis via CCK-8 assay revealed that exogenous
708 AMF acts as a critical survival factor for the gCap-enriched population under hypoxia. Supplementation
709 with recombinant AMF (Hyp + EC + AMF) significantly enhanced cell viability, an effect that closely
710 mimicked the strong viability observed in the co-culture group (Hyp + T/EC). Crucially, this protective
711 effect was strictly dependent on the presence of AMF, as confirmed by the significant impairment of gCap
712 cell viability in the interference co-culture group (Hyp + T/EC + Ad-shGPI), where AMF derived from the
713 CD4 *ATF7IP*$^{+}$-enriched population was silenced (n=3 biological replicates; Figure 5G). This demonstrates
714 that AMF is the primary mediator of the beneficial effects conferred by the CD4 *ATF7IP*$^{+}$-enriched
715 population. Assessment of oxidative stress further corroborated these findings. Intracellular ROS levels
716 exhibited an inverse pattern to cell viability. The ROS levels were lowest in both the recombinant AMF
717 group and the standard co-culture group, confirming that AMF effectively alleviates hypoxia-induced
718 oxidative stress. Notably, the co-culture group yielded slightly lower ROS levels than the recombinant AMF
719 group alone. This suggests that while AMF is the dominant antioxidative factor, the CD4 *ATF7IP*$^{+}$-enriched
720 population likely secretes additional auxiliary cytokines that cooperatively enhance antioxidative regulation
721 (n=3 biological replicates; Figure 5H).

722 To elucidate the molecular mechanisms underlying these protective effects, we investigated the PI3K-
723 AKT signaling axis. This pathway was identified as a primary candidate through KEGG enrichment analyses
724 of both the gCap-enriched population and GPI protein, which highlighted it as a canonical downstream
725 effector of AMF involved in cell survival and metabolism (Supplemental Figure S38E; Supplemental Table
726 S10). To evaluate whether AMF exerts its downstream protective effects via AMFR to activate the PI3K
727 pathway (Park and Jeoung, 2020), which is typically facilitated by the downregulation of Caveolin-1 (Cav-

Uncorrected proof

1, as identified in our DIA quantitative proteomics analysis), we performed receptor-blocking experiments using the functional neutralizing 3F3A mAb. Notably, AMFR blockade largely abolished the ability of AMF to enhance gCap viability and mitigate ROS levels, indicating that AMFR plays a pivotal role in AMF-mediated protection (n=3 biological replicates; Figure 5F and I). Collectively, these results suggest that AMF facilitates the hypoxic adaptation of the gCap-enriched population potentially by interacting with its receptor gp78/AMFR. This process relies on PI3K phosphorylation and the downregulation of Cav-1, which coordinate to promote AKT phosphorylation and subsequent cellular protection.

In summary, our data establish GPI/AMF as a critical paracrine mediator that enhances the metabolic homeostasis and stress resistance of the gCap-enriched population under hypoxic conditions. We demonstrate that AMF facilitates this adaptation likely through interaction with its receptor gp78/AMFR. This interaction appears to depend on PI3K phosphorylation and the concurrent downregulation of Cav-1 expression to promote robust AKT phosphorylation. Ultimately, this orchestrates a dual protective response: promoting cellular activity to maintain the progenitor pool and significantly reducing intracellular ROS levels to prevent oxidative damage. The observation that recombinant AMF protein largely recapitulates the protective phenotype of the co-culture system, whereas GPI silencing abolishes these benefits, confirms that GPI/AMF secreted by the CD4 *ATF7IP*$^{+}$-enriched population plays an indispensable regulatory role in preserving gCap homeostasis.

DISCUSSION

Yaks are well-adapted to the high–altitude ecological environment characterized by cold, low oxygen, high altitude and intense ultraviolet radiation. As a representative organ of yak adaptation to high-altitude environments, there is a large divergence of differential transcripts associated with plateau adaptation in the lungs (Qi et al., 2019), which reflects the critical role of the lungs in directly coping with the low oxygen

Zoological Research

environment and driving adaptive responses. In addition to gas exchange, the lungs act as an important immune barrier (Hurskainen et al., 2021). Therefore, this study focused on the lungs as the organ to explore the high-altitude adaptation of yaks. We systematically constructed the most extensive single-cell transcriptomic landscape of bovine lungs to date, encompassing yak, dzho and cattle. This comprehensive atlas identified 51 subtypes, including 13 previously unrecognized subtypes. Here, these newly identified subtypes are defined as cell clusters with distinct marker expression signatures that have not been previously described in published bovine or mammalian lung single-cell atlases, suggesting potential lineage- or species-specific evolutionary adaptations or physiological acclimatization to high-altitude environments. Furthermore, we explored the cellular mechanisms associated with high-altitude adaptation in yak. In this study, we found that yak and dzho exhibit numerous differentially enriched cell subtypes compared to low-altitude cattle. These differences likely reflect distinct physiological and metabolic adaptations to environmental pressures. These subtypes were significantly more abundant in yak and dzho than in cattle, predominantly within T&NK immune cells.

While our comparative design provides valuable insights into high-altitude biology, the sampling of yaks and dzhos at approximately 3,600 m and cattle at 570 m means that species genetic background and environmental altitude exposure are concurrent variables. Consequently, the observed interspecies differences likely represent a complex interplay of genetically encoded evolutionary adaptation, long-term physiological acclimatization, and other population-specific factors. Additionally, due to the logistical constraints of high-altitude field sampling, lung tissues were cryopreserved prior to enzymatic dissociation without complete pulmonary perfusion. Although this strategy successfully preserved high-quality RNA for robust transcriptional profiling, it may influence the capture efficiency of certain cell populations (e.g.,

Zoological Research

771 fragile epithelial cells or intravascular immune cells). Therefore, the reported cellular proportions should be
772 interpreted as relative abundances within the scRNA-seq libraries rather than absolute *in vivo* compositions.

773 **Differential T&NK subtypes and their association with high-altitude adaptation in yak**

774 T&NK cells are key immune cells in hypoxic immune-related microenvironments (Li et al., 2021). Among
775 the T&NK immune cell subtypes, the 3 new subtypes, CD4 *ATF7IP*$^+$, CD8 *BCL2L11*$^+$, CD8 *TRGC6*$^+$, along
776 with one known subtype, CD4 Th1 like, accounted for a high percentage in yak and dzho. Further analysis
777 of interspecies differences revealed that most of the hypoxia-induced signaling pathways in T&NK subtypes
778 were associated with immune regulation (El Alam et al., 2022; Rodor et al., 2022; Xin et al., 2019), such as
779 T cell receptor signaling pathway, NF-kappa B signaling pathway and IL-17 signaling pathway, all of which
780 showed a significant upregulation trend. The central genes obtained from the differential subtype PPI
781 analysis were also mostly associated with the above pathways.

782 Specifically, the TCR determines the phenotype and function of CD4$^+$ T cells, and TCR signaling plays a
783 crucial role in T cell development, antigen recognition, activation and differentiation processes following
784 presentation of peptide–MHC complexes by antigen-presenting cells (Meitei and Lal, 2023; Pearce, 2010;
785 Zhu, 2018). Members of the nuclear factor-κB (NF-κB) family of transcription factors regulate inflammation
786 and coordinate immune responses and tissue homeostasis (Eltzschig and Carmeliet, 2011). Hypoxia
787 amplifies the NF-κB pathway by increasing the expression and signaling of Toll-like receptors (Mei et al.,
788 2020), thereby potentiating inflammatory signaling cascades that modulate cytokine and chemokine
789 production and leukocyte recruitment (Kuhlicke et al., 2007). The IL-17 axis acts as an important
790 inflammatory effector that functions synergistically with other inflammatory signals synergistically,
791 activating downstream pathways including NFκB and MAPKs (Amatya et al., 2017). Together, these
792 pathway activations are expected to reshape the immune environment and influence endothelial behaviour,

Uncorrected proof

such as barrier function, remodelling and repair, rather than solely serving canonical pathogen-clearing roles (Du et al., 2012; Kwee et al., 2018).

Consistent with this interpretation, our cell–cell communication analysis revealed that the CD4 *ATF7IP*$^{+}$ subtype exhibited the largest number of significant ligand–receptor interactions with the gCap subtype. These findings suggest that the CD4 *ATF7IP*$^{+}$ subtype may potentially contribute to the adaptive phenotype under high-altitude hypoxia by activating gCap proliferation and inflammatory response pathways. In yak lungs, this interaction may enhance gCap-mediated vascular remodelling, improve oxygen transport efficiency and reduce hypoxia-induced inflammatory injury.

Other differential subtypes and their association with high-altitude adaptation in yak

In addition to T&NK cells showing clear interspecies differences, we found that some cell subtypes showed a trend of being more abundant in yak and dzho and less abundant in cattle. These subtypes included the fibroblasts subtypes, the myeloid subtype neutrophils, the B&plasma cell subtype pro B and the endothelial cell subtype gCap.

gCap is a key subtype of pulmonary vascular endothelial cells that specializes in regulating vasodilation and vasoconstriction. As described by Gillich et al. (Gillich et al., 2020), the pulmonary alveolar capillary endothelial cells in mammals consist of a mixture of two cell types: aCap and gCap. aCap specialises in gas exchange and leukocyte transport, whereas gCap specialises in the regulation of vasodilatory tone and functions as a stem/progenitor cell in capillary homeostasis and repair. In our study, gCap (18.14%) accounted for a slightly lower proportion of endothelial cells than aCap (20.05%), and the yak gCap function involved the growth factor receptor signaling pathway and reactive oxygen species metabolism. Thus, we speculated that it may regulate cell proliferation and migration (Rodor et al., 2022) and be closely associated with the plateau adaptability of yak and dzho. Gao et al. (Gao et al., 2022) constructed single-cell

Zoological Research

transcriptional atlas of lung tissues from yak and cattle and identified a yak-specific endothelial cell cluster without specific nomenclature or characterisation. They hypothesised that this cluster may be associated with plateau adaptation in yak, and this cluster may correspond to the gCap subtype in this study.

CD4 *ATF7IP*$^{+}$ regulate gCap homeostasis via the GPI/AMF axis

The intimate crosstalk between immune and vascular systems stem from their shared evolutionary origins, where common progenitors diverged into specialized lineages to maintain tissue homeostasis (Amersfoort et al., 2022). In the pulmonary vasculature, the gCap subtype acts as a stem-like progenitor essential for microvascular maintenance and repair (Gillich et al., 2020; Yang et al., 2024). Localized within alveolar septa, gCaps possess a rapid proliferative capacity, allowing them to replenish endothelial pools. Consequently, preserving the regenerative potential of gCaps is paramount for pulmonary adaptation to environmental stress.

As central coordinators of vascular homeostasis, CD4^{+} T cells modulate endothelial proliferation, migration, permeability and metabolic stability under both immune and non-immune conditions (Certo et al., 2021). Specifically, this regulation is dictated by distinct cytokine axes: Th1-derived IFN-γ typically inhibits angiogenesis (Jorgovanovic et al., 2020), while Th2 cytokines (IL-4, IL-13) facilitate endothelial repair (Espinosa Gonzalez et al., 2022), and Th17-secreted IL-17 promotes VEGF expression to enhance angiogenic activity (Du et al., 2012; Kwee et al., 2018; Pan et al., 2015).

Despite these insights, direct evidence linking CD4^{+} T cells to the specific regulation of the stem-like gCap subtype remains elusive. Given the regenerative potency of gCaps, their interaction with the adaptive immune system likely constitutes a fundamental yet undefined mechanism governing lung homeostasis. This crosstalk could potentially involve several pathways, such as the modulation of the Apelin−APJ axis (Godoy et al., 2023) or direct MHC II-mediated communication (Mora Massad et al., 2025). Additionally, hypoxia-

Uncorrected proof

induced NF-κB signaling may help balance oxidative stress and inflammatory responses during this cellular interaction (Castillo-Rodríguez et al., 2022; Xue et al., 2023). To resolve the precise molecular mechanisms behind this process, it is essential to pinpoint the specific paracrine factors secreted by $CD4^+$ T cells that drive gCap adaptation under hypoxia.

To identify the specific mediators driving this interaction, we performed proteomic analysis to screen five candidate cytokines that are potentially secreted by the CD4 *ATF7IP*$^+$-enriched population, including F10, LDHA, GPI, TPM2 and IL1B. Among these, GPI (glucose-6-phosphate isomerase) appeared to be the most valuable target, owing to its dual function as both a metabolic enzyme and a signalling molecule. Intracellularly, GPI acts as a pivotal metabolic enzyme in glycolysis and gluconeogenesis. Conversely, its extracellular form functions as a cytokine known as autocrine motility factor (AMF) (Haga et al., 2000). Unlike classical cytokines, AMF lacks a signal peptide and relies on a non-classical secretion pathway, which is typically activated in the context of tumor cells or upon lectin stimulation in T cells (Faik et al., 1988; Haga et al., 2000; Yanagawa et al., 2004). Consistent with this regulatory mechanism, we found that AMF release was minimal under hypoxia alone but was profoundly induced in the co-culture system. This indicates that the crosstalk with the gCap subtype acts as the essential trigger for AMF secretion by $CD4^+$ T cells.

Accumulating evidence has established that AMF is a multifunctional cytokine involved in cell growth, differentiation, survival and motility, and plays an important role in in tumor progression and metastasis (Funasaka et al., 2001; Nabi et al., 1992; Tsutsumi et al., 2003b). In this study, we identified a novel role for AMF in facilitating the hypoxic adaptation of the gCap subtype, observing that AMF treatment markedly enhances gCap viability and suppresses ROS accumulation under hypoxia, a finding consistent with its characterization as a non-classical angiogenic factor. The PI3K/Akt signaling axis emerged as the primary

Zoological Research

candidate, as integrated KEGG enrichment analyses of both the gCap subtype and GPI protein consistently highlighted it as a canonical downstream effector of AMF.

At the molecular level, the biological function of AMF is initiated by its interaction with the cell surface receptor gp78/AMFR, a 78 kDa glycoprotein (Fairbank et al., 2009; Silletti and Raz, 1993). While AMF can engage alternate binding partners like IGFBP-3 (Mishra et al., 2004) or HER2 (Kho et al., 2013), indicating a cell-type-specific response, it is likely that its role in gCap adaptation is mediated by the canonical receptor gp78/AMFR. Notably, recombinant AMF-stimulated gCap viability peaked at 0.2 μg/mL and plateaued at higher doses (0.4−1.5 μg/mL), representing a receptor saturation-mediated safety brake that prevents cellular over-stimulation under hypoxic stress. Mechanistically, previous studies have shown that the signal transduction triggered by AMF-receptor engagement relies on specific endocytic trafficking. Following its interaction with gp78/AMFR, AMF induces the activation of the PI3K/Akt pathway. Although AMF can be internalized via distinct routes, established models indicate that the pathway relevant to cell survival is a raft-dependent, dynamin-dependent process that targets the smooth endoplasmic reticulum (SER). Crucially, this SER-targeting pathway is governed by the opposing regulatory effects of Cav-1 (a negative regulator) (Benlimame et al., 1998; Le et al., 2002; Shankar et al., 2013) and PI3K (a positive regulator) (Kojic et al., 2007; Kojic et al., 2008; Tsutsumi et al., 2003a). The concurrent activation of PI3K and downregulation of Cav-1 observed in our study may therefore provide the molecular basis for the PI3K-dependent internalization of the AMF−gp78/AMFR complex, thereby driving the pro-survival and viability-enhancing effects observed in gCaps under hypoxia. It should be noted that regarding our *in vitro* functional assays demonstrating this axis, the absence of an empty-vector control (Ad-NC) in the *GPI* knockdown experiments means that potential non-specific effects caused by adenoviral transduction cannot be definitively excluded.

Zoological Research

However, the consistent protective effects observed with exogenous recombinant AMF supplementation strongly support its major role in this regulatory mechanism.

In addition to enhancing cellular viability, the AMF−gp78/AMFR axis is also a critical driver of angiogenesis (Nabi et al., 1992; Yanagawa et al., 2004). *In vivo* studies demonstrate that stable AMF overexpression markedly enhances capillary vessel formation (Funasaka et al., 2001). This angiogenic potential is likely mediated by crosstalk with the VEGF signaling axis. Notably, paracrine AMF stimulation in endothelial cells has been shown to upregulate the VEGF receptor Flt-1 via a PKC- and PI3K-dependent signaling cascade (Funasaka et al., 2002). This suggests that AMF may further support gCap function by potentiating their sensitivity to angiogenic signals.

Alongside its role in cell growth, AMF/PGI is recognized for its potent cytoprotective effects under environmental stress (Tsutsumi et al., 2003a). Previous studies have characterized its ability to suppress apoptosis via the PI3K/Akt signaling pathway by downregulating pro-apoptotic factors such as Apaf-1 and caspase-9 (Fu et al., 2011; Haga et al., 2003). However, the upstream events initiating this survival advantage remain to be fully elucidated. Given that PI3K/Akt is a central regulator of redox homeostasis (Tian et al., 2015; Wang et al., 2008), and that excessive ROS accumulation serves as a primary trigger for hypoxia-induced apoptosis and ER stress (Cao and Kaufman, 2014; Redza-Dutordoir and Averill-Bates, 2016), we investigated whether AMF confers protection by mitigating oxidative stress. Our findings demonstrate that AMF treatment concurrently activates Akt and markedly reduces intracellular ROS levels. This suggests that AMF-mediated PI3K/Akt signaling promotes gCap adaptation not only through classical survival signaling but also by buffering against oxidative stress, which effectively pre-empts the activation of downstream apoptotic cascades.

Uncorrected proof

Within the co-culture system of the CD4 *ATF7IP*$^{+}$-enriched and gCap-enriched populations, AMF functions in coordination with other cytokines to regulate antioxidant responses and hypoxic adaptation. Interleukin-1 β (IL-1β) is a notable candidate for this interaction (Kidder et al., 2024), as it is recognized for its ability to modulate endothelial inflammation and angiogenesis (Marceau et al., 1992; Wilson et al., 2007). Although primarily associated with myeloid cells (Pulugulla et al., 2018), activated CD4^{+} T cells produce mature IL-1β to influence the local microenvironment (Arbore et al., 2016; Doitsh et al., 2014). Our proteomic analysis identified elevated IL-1β levels in both the CD4 *ATF7IP*$^{+}$-enriched and gCap-enriched populations, which indicates that AMF and IL-1β signaling collectively promote gCap survival. This combined signaling maintains pulmonary homeostasis under hypoxic stress.

Based on our findings and existing literature, we propose a novel model for immune-vascular adaptation in the plateau environment. Under hypoxic stress, interaction with the gCap subtype triggers the CD4 ATF7IP^{+} subtype to secrete GPI/AMF. This paracrine AMF likely interacts with gp78/AMFR on the gCap subtype, potentially initiating a specific endocytic program characterized by PI3K activation and Cav-1 suppression. This process is thought to facilitate the transport of the AMF-receptor complex to the SER. Downstream of this event, the PI3K/Akt axis serves a dual purpose: it enhances metabolic activity and viability to maintain the progenitor pool and orchestrates a robust antioxidant response to reduce ROS accumulation. Through this coordinated regulation of metabolic activity, cell viability and oxidative stress resistance, the CD4 *ATF7IP*$^{+}$ subtype maintains gCap homeostasis. This mechanism likely facilitates efficient vascular remodeling and oxygen transport under plateau hypoxia, offering a potential therapeutic target for high-altitude-related vascular disorders.

Uncorrected proof

CONCLUSION

Overall, this study establishes the most comprehensive single-cell transcriptomic atlas of yak, dzho and cattle lungs to date, encompassing 51 cell subtypes and identifying 13 novel subtypes primarily distributed within the T&NK cell population. We elucidated an immune-endothelial axis where the CD4 *ATF7IP*$^{+}$ subtype regulates gCap function under hypoxia via the secretion of GPI/AMF. This paracrine mediator likely interacts with its receptor AMFR/gp78 to trigger a signaling cascade that appears to depend on PI3K phosphorylation to drive AKT activation, which effectively suppresses ROS accumulation and maintains gCap survival. These findings provide key insights into the cellular and molecular basis of pulmonary vascular adaptation in bovines and offer a valuable transcriptomic resource for future studies on hypoxia adaptation and genetic improvement in livestock.

SUPPLEMENTARY DATA

Supplementary data for this article can be found online.

ABBREVIATIONS

scRNA: Single-cell RNA sequencing; STRING: Search Tool for the Retrieval of Interacting Genes; TFs: Transcription Factors; UMAP: Uniform Manifold Approximation and Projection. MNNs: Mutual Nearest Neighbours; PCA: Principal Component Analysis; SNN: Shared Nearest Neighbour; ANOVA: Analysis of Variance; MOD: Mean Optical Density; FBS: Fetal Bovine Serum; PPI: protein-protein interaction; GO: Gene Ontology; KEGG: Kyoto Encyclopedia of Genes and Genomes; GSVA: Gene Set Variation Analysis; WB: Western Blot; IHC: Immunohistochemistry; IF: Immunofluorescence; FACS: Fluorescence-activated cell sorting; AMF: Autocrine motility factor; SER: Smooth endoplasmic reticulum.

DATA AVAILABILITY

The single-cell RNA sequencing data generated in this study have been submitted to the NCBI Gene

Uncorrected proof

Expression Omnibus (GEO; https://www.ncbi.nlm.nih.gov/geo/) under accession number GSE266061. All other datasets generated and/or analyzed during the current study are available from the corresponding author upon request.

COMPETING INTEREST

Authors declare that they have no competing interests.

AUTHOR CONTRIBUTIONS

Conceptualization: R.Z., D.L.; Methodology: R.Z., D.L.; Validation: R.Z.; Formal analysis: R.Z.; Investigation: R.Z.; Resources: Q.Z., D.Y., J.W., M.X., S.Y., W.J., Y.X., T.-D.M., J.L., W.B.; Data curation: R.Z.; Writing—original draft: R.Z.; Writing—review & editing: R.Z., D.L., W.F.; Visualization: R.Z.; Supervision: D.L.; Project administration: D.L.; Funding acquisition: D.L., R.Z. All authors contributed to and have approved the manuscript.

REFERENCES

Amatya N, Garg AV, Gaffen SL. 2017. IL-17 signaling: the yin and the yang. *Trends Immunol*, **38**(5): 310-322.

Amersfoort J, Eelen G, Carmeliet P. 2022. Immunomodulation by endothelial cells - Partnering up with the immune system? *Nat Rev Immunol*, **22**(9): 576-588.

Araki K, Shimura T, Yajima T, Tsutsumi S, Suzuki H, Okada K, etc. 2009. Phosphoglucose isomerase/autocrine motility factor promotes melanoma cell migration through ERK activation dependent on autocrine production of interleukin-8. *J Biol Chem*, **284**(47): 32305-32311.

Arbore G, West EE, Spolski R, Robertson AaB, Klos A, Rheinheimer C, etc. 2016. T helper 1 immunity requires complement-driven NLRP3 inflammasome activity in $CD4^+$ T cells. *Science*, **352**(6292): aad1210.

Zoological Research

965 Benlimame N, Le PU, Nabi IR. 1998. Localization of autocrine motility factor receptor to caveolae and
966 clathrin-independent internalization of its ligand to smooth endoplasmic reticulum. *Mol Biol Cell*, **9**(7):
967 1773-1786.
968 Buechler MB, Pradhan RN, Krishnamurty AT, Cox C, Calviello AK, Wang AW, etc. 2021. Cross-tissue
969 organization of the fibroblast lineage. *Nature*, **593**(7860): 575-579.
970 Cao SS & Kaufman RJ. 2014. Endoplasmic reticulum stress and oxidative stress in cell fate decision
971 and human disease. *Antioxid Redox Signal*, **21**(3): 396-413.
972 Castillo-Rodríguez RA, Trejo-Solís C, Cabrera-Cano A, Gómez-Manzo S, Dávila-Borja VM. 2022.
973 Hypoxia as a modulator of inflammation and immune response in cancer. *Cancers (Basel)*, **14**(9).
974 Certo M, Elkafrawy H, Pucino V, Cucchi D, Cheung KCP, Mauro C. 2021. Endothelial cell and T-cell
975 crosstalk: Targeting metabolism as a therapeutic approach in chronic inflammation. *Br J Pharmacol*,
976 **178**(10): 2041-2059.
977 Doitsh G, Galloway NL, Geng X, Yang Z, Monroe KM, Zepeda O, etc. 2014. Cell death by pyroptosis
978 drives CD4 T-cell depletion in HIV-1 infection. *Nature*, **505**(7484): 509-514.
979 Du JW, Xu KY, Fang LY, Qi XL. 2012. Interleukin-17, produced by lymphocytes, promotes tumor growth
980 and angiogenesis in a mouse model of breast cancer. *Mol Med Rep*, **6**(5): 1099-1102.
981 El Alam S, Pena E, Aguilera D, Siques P, Brito J. 2022. Inflammation in pulmonary hypertension and
982 edema induced by hypobaric hypoxia exposure. *Int J Mol Sci*, **23**(20).
983 Eltzschig HK & Carmeliet P. 2011. Hypoxia and inflammation. *N Engl J Med*, **364**(7): 656-665.
984 Espinosa Gonzalez M, Volk-Draper L, Bhattarai N, Wilber A, Ran S. 2022. Th2 cytokines IL-4, IL-13,
985 and IL-10 promote differentiation of pro-lymphatic progenitors derived from bone marrow myeloid
986 precursors. *Stem Cells Dev*, **31**(11-12): 322-333.

Uncorrected proof

987 Faik P, Walker JI, Redmill AA, Morgan MJ. 1988. Mouse glucose-6-phosphate isomerase and
988 neuroleukin have identical 3' sequences. *Nature*, **332**(6163): 455-457.
989 Fairbank M, St-Pierre P, Nabi IR. 2009. The complex biology of autocrine motility
990 factor/phosphoglucose isomerase (AMF/PGI) and its receptor, the gp78/AMFR E3 ubiquitin ligase.
991 *Mol Biosyst*, **5**(8): 793-801.
992 Fu M, Li L, Albrecht T, Johnson JD, Kojic LD, Nabi IR. 2011. Autocrine motility factor/phosphoglucose
993 isomerase regulates ER stress and cell death through control of ER calcium release. *Cell Death*
994 *Differ*, **18**(6): 1057-1070.
995 Funasaka T, Haga A, Raz A, Nagase H. 2001. Tumor autocrine motility factor is an angiogenic factor
996 that stimulates endothelial cell motility. *Biochem Biophys Res Commun*, **285**(1): 118-128.
997 Funasaka T, Haga A, Raz A, Nagase H. 2002. Tumor autocrine motility factor induces
998 hyperpermeability of endothelial and mesothelial cells leading to accumulation of ascites fluid.
999 *Biochem Biophys Res Commun*, **293**(1): 192-200.
1000 Gao X, Wang S, Wang YF, Li S, Wu SX, Yan RG, etc. 2022. Long read genome assemblies
1001 complemented by single cell RNA-sequencing reveal genetic and cellular mechanisms underlying
1002 the adaptive evolution of yak. *Nat Commun*, **13**(1): 4887.
1003 Gillich A, Zhang F, Farmer CG, Travaglini KJ, Tan SY, Gu M, etc. 2020. Capillary cell-type specialization
1004 in the alveolus. *Nature*, **586**(7831): 785-789.
1005 Godoy RS, Cober ND, Cook DP, Mccourt E, Deng Y, Wang L, etc. 2023. Single-cell transcriptomic atlas
1006 of lung microvascular regeneration after targeted endothelial cell ablation. *Elife*, **12**.
1007 Haga A, Funasaka T, Niinaka Y, Raz A, Nagase H. 2003. Autocrine motility factor signaling induces
1008 tumor apoptotic resistance by regulations Apaf-1 and Caspase-9 apoptosome expression. *Int J*

Uncorrected proof

Cancer, **107**(5): 707-714.

Haga A, Niinaka Y, Raz A. 2000. Phosphohexose isomerase/autocrine motility factor/neuroleukin/maturation factor is a multifunctional phosphoprotein. *Biochim Biophys Acta*, **1480**(1-2): 235-244.

Hurskainen M, Mižíková I, Cook DP, Andersson N, Cyr-Depauw C, Lesage F, etc. 2021. Single cell transcriptomic analysis of murine lung development on hyperoxia-induced damage. *Nat Commun*, **12**(1): 1565.

Jorgovanovic D, Song M, Wang L, Zhang Y. 2020. Roles of IFN-γ in tumor progression and regression: a review. *Biomark Res*, **8**: 49.

Kho DH, Nangia-Makker P, Balan V, Hogan V, Tait L, Wang Y, etc. 2013. Autocrine motility factor promotes HER2 cleavage and signaling in breast cancer cells. *Cancer Res*, **73**(4): 1411-1419.

Kidder E, Gangopadhyay S, Francis S, Alfaidi M. 2024. "How to release or not release, that is the question." A review of interleukin-1 cellular release mechanisms in vascular inflammation. *J Am Heart Assoc*, **13**(5): e032987.

Kojic LD, Joshi B, Lajoie P, Le PU, Cox ME, Turbin DA, etc. 2007. Raft-dependent endocytosis of autocrine motility factor is phosphatidylinositol 3-kinase-dependent in breast carcinoma cells. *J Biol Chem*, **282**(40): 29305-29313.

Kojic LD, Wiseman SM, Ghaidi F, Joshi B, Nedev H, Saragovi HU, etc. 2008. Raft-dependent endocytosis of autocrine motility factor/phosphoglucose isomerase: a potential drug delivery route for tumor cells. *PLoS One*, **3**(10): e3597.

Kuhlicke J, Frick JS, Morote-Garcia JC, Rosenberger P, Eltzschig HK. 2007. Hypoxia inducible factor (HIF)-1 coordinates induction of Toll-like receptors TLR2 and TLR6 during hypoxia. *PLoS One*, **2**(12):

Uncorrected proof

e1364.

Kwee BJ, Budina E, Najibi AJ, Mooney DJ. 2018. CD4 T-cells regulate angiogenesis and myogenesis. *Biomaterials*, **178**: 109-121.

Le PU, Guay G, Altschuler Y, Nabi IR. 2002. Caveolin-1 is a negative regulator of caveolae-mediated endocytosis to the endoplasmic reticulum. *J Biol Chem*, **277**(5): 3371-3379.

Li X, Cai H, Cai Y, Zhang Q, Ding Y, Zhuang Q. 2021. Investigation of a hypoxia-immune-related microenvironment gene signature and prediction model for idiopathic pulmonary fibrosis. *Front Immunol*, **12**: 629854.

Lin K, Ye P, Liu J, He F, Xu W. 2015. Endostar inhibits hypoxia-induced cell proliferation and migration via the hypoxia-inducible factor-1α/vascular endothelial growth factor pathway *in vitro*. *Mol Med Rep*, **11**(5): 3780-3785.

Long L, Zhu Y, Li Z, Zhang H, Liu L, Bai J. 2020. Differential expression of skeletal muscle mitochondrial proteins in yak, dzo, and cattle: a proteomics-based study. *J Vet Med Sci*, **82**(8): 1178-1186.

Marceau F, Grassi J, Frobert Y, Bergeron C, Poubelle PE. 1992. Effects of experimental conditions on the production of interleukin-1 alpha and -1 beta by human endothelial cells cultured *in vitro*. *Int J Immunopharmacol*, **14**(4): 525-534.

Maron BA, Oldham WM, Chan SY, Vargas SO, Arons E, Zhang YY, etc. 2014. Upregulation of steroidogenic acute regulatory protein by hypoxia stimulates aldosterone synthesis in pulmonary artery endothelial cells to promote pulmonary vascular fibrosis. *Circulation*, **130**(2): 168-179.

Mei L, Zheng YM, Song T, Yadav VR, Joseph LC, Truong L, etc. 2020. Rieske iron-sulfur protein induces FKBP12.6/RyR2 complex remodeling and subsequent pulmonary hypertension through NF-κB/cyclin D1 pathway. *Nat Commun*, **11**(1): 3527.

uncorrected proof

Meitei HT & Lal G. 2023. T cell receptor signaling in the differentiation and plasticity of CD4+ T cells. *Cytokine & Growth Factor Reviews*, **69**: 14-27.

Mishra S, Raz A, Murphy LJ. 2004. Insulin-like growth factor binding protein-3 interacts with autocrine motility factor/phosphoglucose isomerase (AMF/PGI) and inhibits the AMF/PGI function. *Cancer Res*, **64**(7): 2516-2522.

Mora Massad K, Dai Z, Petrache I, Ventetuolo CE, Lahm T. 2025. Lung endothelial cell heterogeneity in health and pulmonary vascular disease. *Am J Physiol Lung Cell Mol Physiol*, **328**(6): L877-l884.

Nabi IR, Watanabe H, Raz A. 1990. Identification of B16-F1 melanoma autocrine motility-like factor receptor. *Cancer Res*, **50**(2): 409-414.

Nabi IR, Watanabe H, Raz A. 1992. Autocrine motility factor and its receptor: role in cell locomotion and metastasis. *Cancer Metastasis Rev*, **11**(1): 5-20.

Pan B, Shen J, Cao J, Zhou Y, Shang L, Jin S, etc. 2015. Interleukin-17 promotes angiogenesis by stimulating VEGF production of cancer cells via the STAT3/GIV signaling pathway in non-small-cell lung cancer. *Sci Rep*, **5**: 16053.

Park HS & Jeoung NH. 2020. Autocrine motility factor secreted by HeLa cells inhibits the growth of many cancer cells by regulating AKT/ERK signaling. *Biochem Biophys Res Commun*, **525**(3): 557-562.

Pearce EL. 2010. Metabolism in T cell activation and differentiation. *Current Opinion in Immunology*, **22**(3): 314-320.

Pulugulla SH, Packard TA, Galloway NLK, Grimmett ZW, Doitsh G, Adamik J, etc. 2018. Distinct mechanisms regulate *IL1B* gene transcription in lymphoid CD4 T cells and monocytes. *Cytokine*, **111**: 373-381.

Uncorrected proof

Qi X, Zhang Q, He Y, Yang L, Zhang X, Shi P, etc. 2019. The transcriptomic landscape of yaks reveals molecular pathways for high altitude adaptation. *Genome Biol Evol*, **11**(1): 72-85.

Qiu Q, Zhang G, Ma T, Qian W, Wang J, Ye Z, etc. 2012. The yak genome and adaptation to life at high altitude. *Nat Genet*, **44**(8): 946-949.

Redza-Dutordoir M & Averill-Bates DA. 2016. Activation of apoptosis signalling pathways by reactive oxygen species. *Biochim Biophys Acta*, **1863**(12): 2977-2992.

Rodor J, Chen SH, Scanlon JP, Monteiro JP, Caudrillier A, Sweta S, etc. 2022. Single-cell RNA sequencing profiling of mouse endothelial cells in response to pulmonary arterial hypertension. *Cardiovasc Res*, **118**(11): 2519-2534.

Shankar J, Kojic LD, St-Pierre P, Wang PT, Fu M, Joshi B, etc. 2013. Raft endocytosis of AMF regulates mitochondrial dynamics through Rac1 signaling and the Gp78 ubiquitin ligase. *J Cell Sci*, **126**(Pt 15): 3295-3304.

Silletti S & Raz A. 1993. Autocrine motility factor is a growth factor. *Biochem Biophys Res Commun*, **194**(1): 446-457.

Tian K, Zhong W, Zheng X, Zhang J, Liu P, Zhang W, etc. 2015. Neuroleukin/Autocrine Motility Factor Receptor Pathway Promotes Proliferation of Articular Chondrocytes through Activation of AKT and Smad2/3. *Sci Rep*, **5**: 15101.

Travaglini KJ, Nabhan AN, Penland L, Sinha R, Gillich A, Sit RV, etc. 2020. A molecular cell atlas of the human lung from single-cell RNA sequencing. *Nature*, **587**(7835): 619-625.

Tsutsumi S, Hogan V, Nabi IR, Raz A. 2003a. Overexpression of the autocrine motility factor/phosphoglucose isomerase induces transformation and survival of NIH-3T3 fibroblasts. *Cancer Res*, **63**(1): 242-249.

Uncorrected proof

Tsutsumi S, Yanagawa T, Shimura T, Fukumori T, Hogan V, Kuwano H, etc. 2003b. Regulation of cell proliferation by autocrine motility factor/phosphoglucose isomerase signaling. *J Biol Chem*, **278**(34): 32165-32172.

Wang D, Zhang H, Li M, Frid MG, Flockton AR, Mckeon BA, etc. 2014. MicroRNA-124 controls the proliferative, migratory, and inflammatory phenotype of pulmonary vascular fibroblasts. *Circ Res*, **114**(1): 67-78.

Wang K, Yang Y, Wang L, Ma T, Shang H, Ding L, etc. 2016. Different gene expressions between cattle and yak provide insights into high-altitude adaptation. *Anim Genet*, **47**(1): 28-35.

Wang L, Chen Y, Sternberg P, Cai J. 2008. Essential roles of the PI3 kinase/Akt pathway in regulating Nrf2-dependent antioxidant functions in the RPE. *Invest Ophthalmol Vis Sci*, **49**(4): 1671-1678.

Wilson HL, Varcoe RW, Stokes L, Holland KL, Francis SE, Dower SK, etc. 2007. P2X receptor characterization and IL-1/IL-1Ra release from human endothelial cells. *Br J Pharmacol*, **151**(1): 115-127.

Xin JW, Chai ZX, Zhang CF, Zhang Q, Zhu Y, Cao HW, etc. 2019. Transcriptome profiles revealed the mechanisms underlying the adaptation of yak to high-altitude environments. *Sci Rep*, **9**(1): 7558.

Xue J, Zhang Z, Sun Y, Jin D, Guo L, Li X, etc. 2023. Research progress and molecular mechanisms of endothelial cells inflammation in vascular-related diseases. *J Inflamm Res*, **16**: 3593-3617.

Yanagawa T, Funasaka T, Tsutsumi S, Watanabe H, Raz A. 2004. Novel roles of the autocrine motility factor/phosphoglucose isomerase in tumor malignancy. *Endocr Relat Cancer*, **11**(4): 749-759.

Yang R, Zheng T, Xiang H, Liu M, Hu K. 2024. Lung single-cell RNA profiling reveals response of pulmonary capillary to sepsis-induced acute lung injury. *Front Immunol*, **15**: 1308915.

Zhu J. 2018. T helper cell differentiation, heterogeneity, and plasticity. *Cold Spring Harb Perspect Biol*,

Uncorrected proof

1119 **10**(10).

uncorrected proof

FIGURES

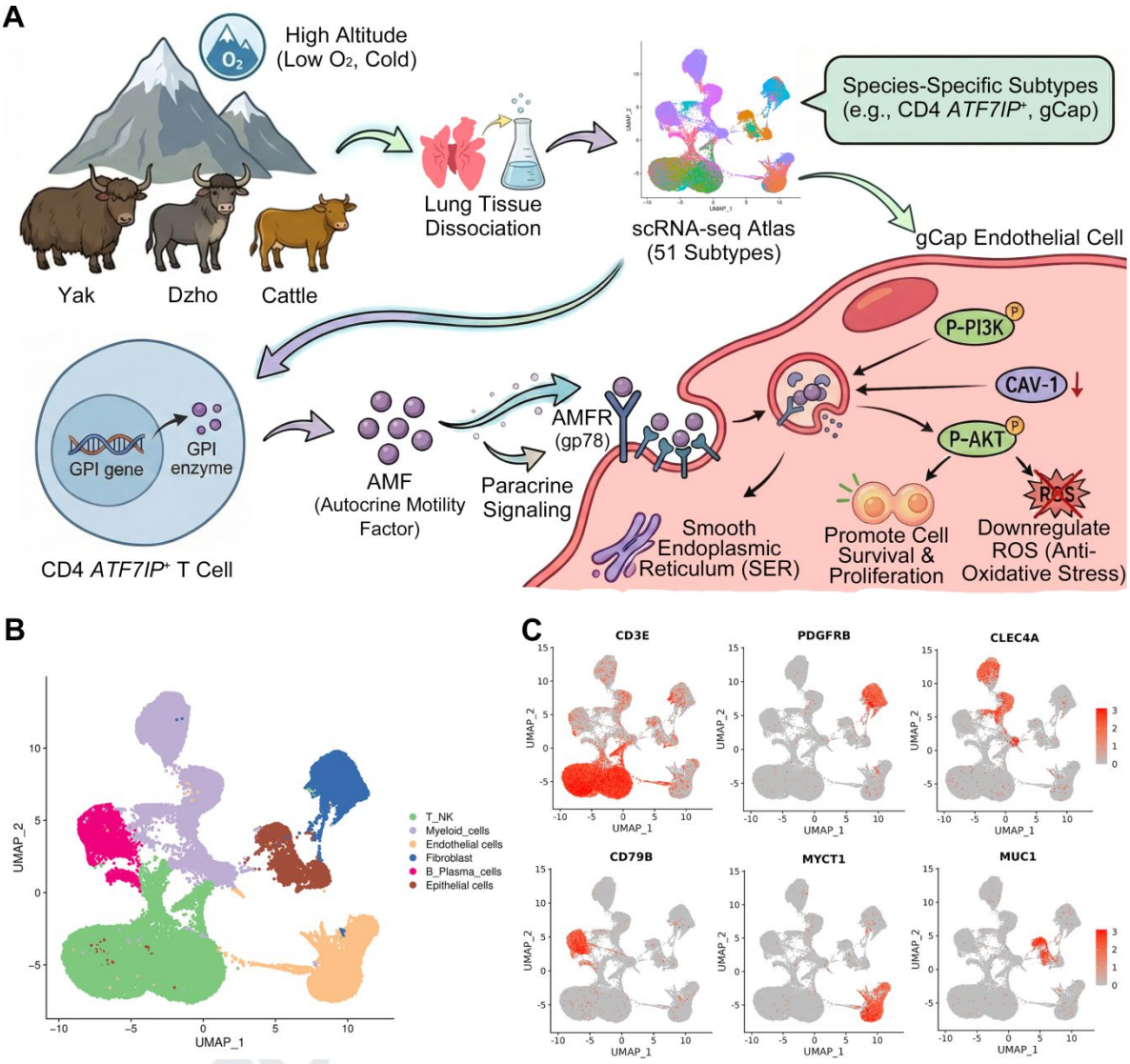


Figure 1. Single-cell atlas of the lungs of bovine species, major cell types.

(**A**) Flowchart showing the construction of a single-cell transcriptome map of bovine lung and further exploration of the data. (**B**) UMAP plot of the main cell types of bovine lung (including yak, dzho and cattle), with cell types coloured as shown in the legend. (**C**) UMAP plot showing the expression levels of typical markers for the T&NK, myeloid, endothelial, fibroblastic, B&Plasma and epithelial cell types, with the intensity of the expression indicated in red.

Zoological Research

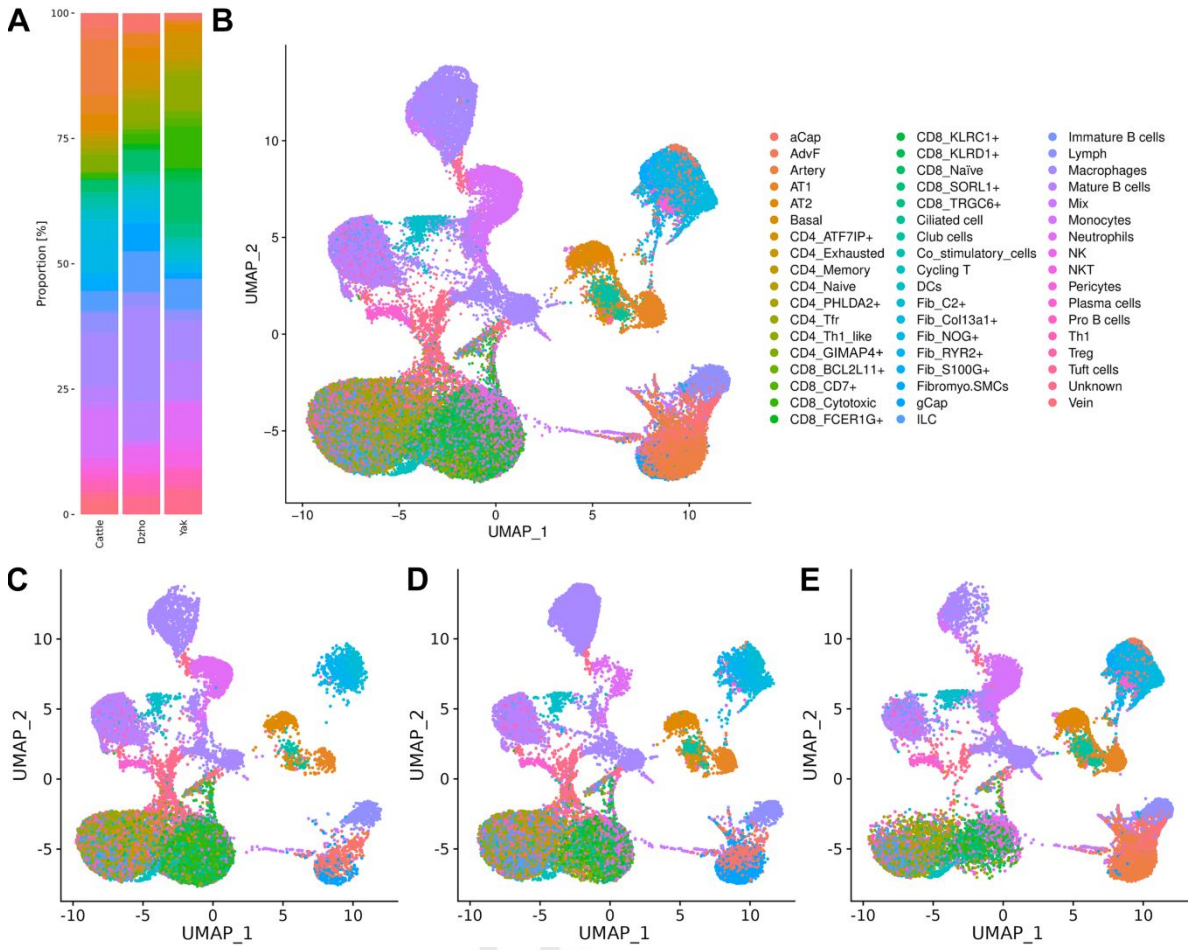
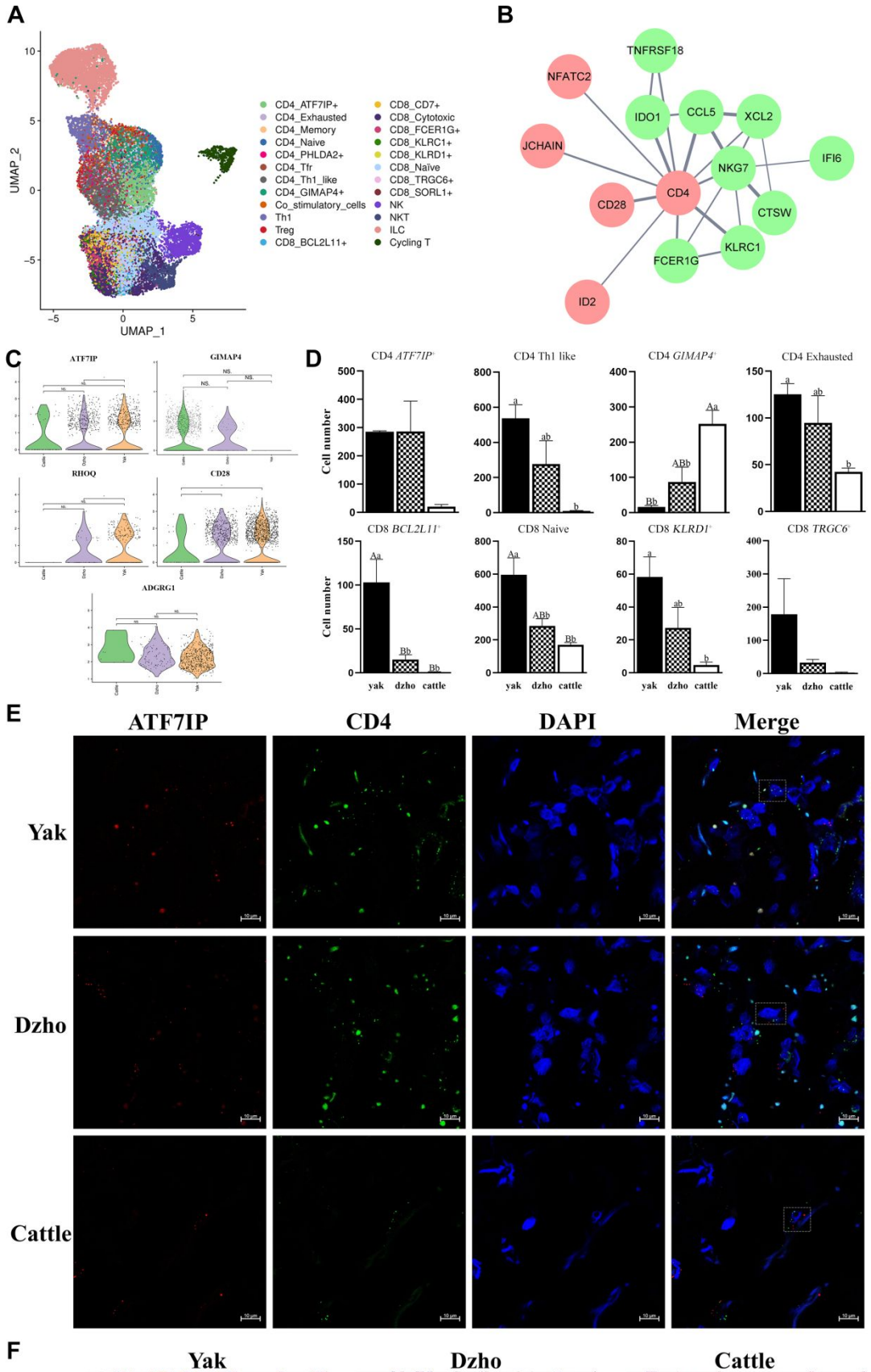


Figure 2. Single-cell transcriptional profiles of the lungs of yak, dzho and cattle

(**A**) Percentage of all cell subtypes in the lungs of yak, dzho and cattle. (**B**) UMAP plots of all scRNA-seq data showing a total of 51 cell types identified. (**C** to **E**) UMAP plots of cell subtypes in the lungs of yak, dzho and cattle, respectively. Cell subtypes are coloured as shown in Figure 2B legend.

uncorrec



Zoological Research

Figure 3. Cell composition of T&NK subtypes in the lungs of yak, dzho and cattle

(**A**) UMAP plot of T&NK immune cell subtypes in the lungs of bovid species, with cell clusters coloured as indicated in the legend. (**B**) PPI network diagram of differential proteins of CD4 *ATF7IP*$^+$, CD8 *BCL2L11*$^+$, CD8 *TRGC6*$^+$ and CD4 Th1 like versus other T&NK subtypes of differential proteins, with upregulated proteins in red and downregulated proteins in green. (**C**) Violin plots showing the expression of selected T&NK subtype marker genes in yak, dzho and cattle. (**D**) Differences in cell numbers of some T&NK immune cell subtypes in yak, dzho and cattle, with error bars representing mean (SEM), labelling all differences at $P<0.05$; different uppercase and lowercase letters between groups indicate $P<0.01$ and $P<0.05$, respectively. (**E**) RNA fluorescence in situ hybridization images of the CD4 *ATF7IP*$^+$ subtype-specific marker gene *ATF7IP* (red) and the CD4$^+$ T cell marker gene *CD4* (green) in yak, dzho and cattle. Magnification: 63×. Scale bars=10 μm. (**F**) Immunohistochemical staining images of CD4 *ATF7IP*$^+$ subtype-specific marker protein MCAF (ATF7IP) in yak, dzho and cattle. Scale bars=50 μm.

uncorrected proof

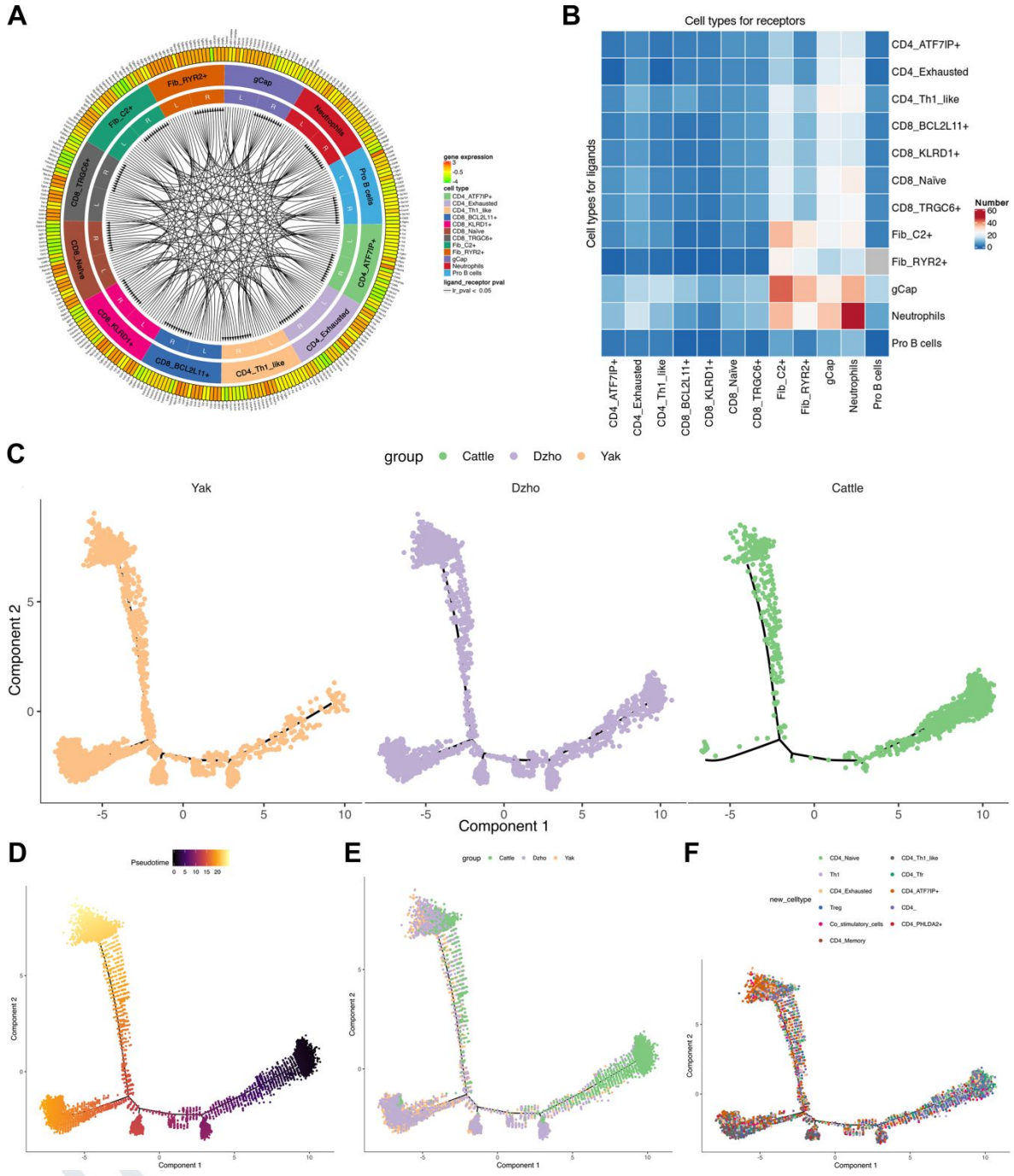


Figure 4. Cell communication and pseudotime in some subtypes of lungs of bovine species

(**A**) Circos plot of the cell communication network, with the outermost circle indicating the expression of ligand/receptor genes (yellow to red indicate low to high expression), the second circle indicating the cell type and the innermost circle indicating the interactions between ligand and receptor gene pairs. Solid lines indicate significant interactions, and dashed lines indicate non-significant interactions. (**B**) Heatmap showing the intensity of interactions between cell types based on the number of ligands or receptors, with the number of ligands or

Zoological Research

receptors from small to large indicated by a colour gradient from blue to red. (**C**) Cell trajectory plots of $CD4^+$ T subtypes in yak, dzho and cattle, with species coloured as indicated in the legend. (**D**) Diagram of the pseudo-temporal trajectories of $CD4^+$ T cells, with colours transitioning from dark to light, representing the timeline of differentiation from early to late stages. (**E**) Cell trajectory display of $CD4^+$ T cell subtypes in yak, dzho and cattle, with species colours as indicated in the legend. (**F**) Cell trajectory display for all subtypes of $CD4^+$ T cells, with the colours of cell types as shown in the legend.

uncorrected proof

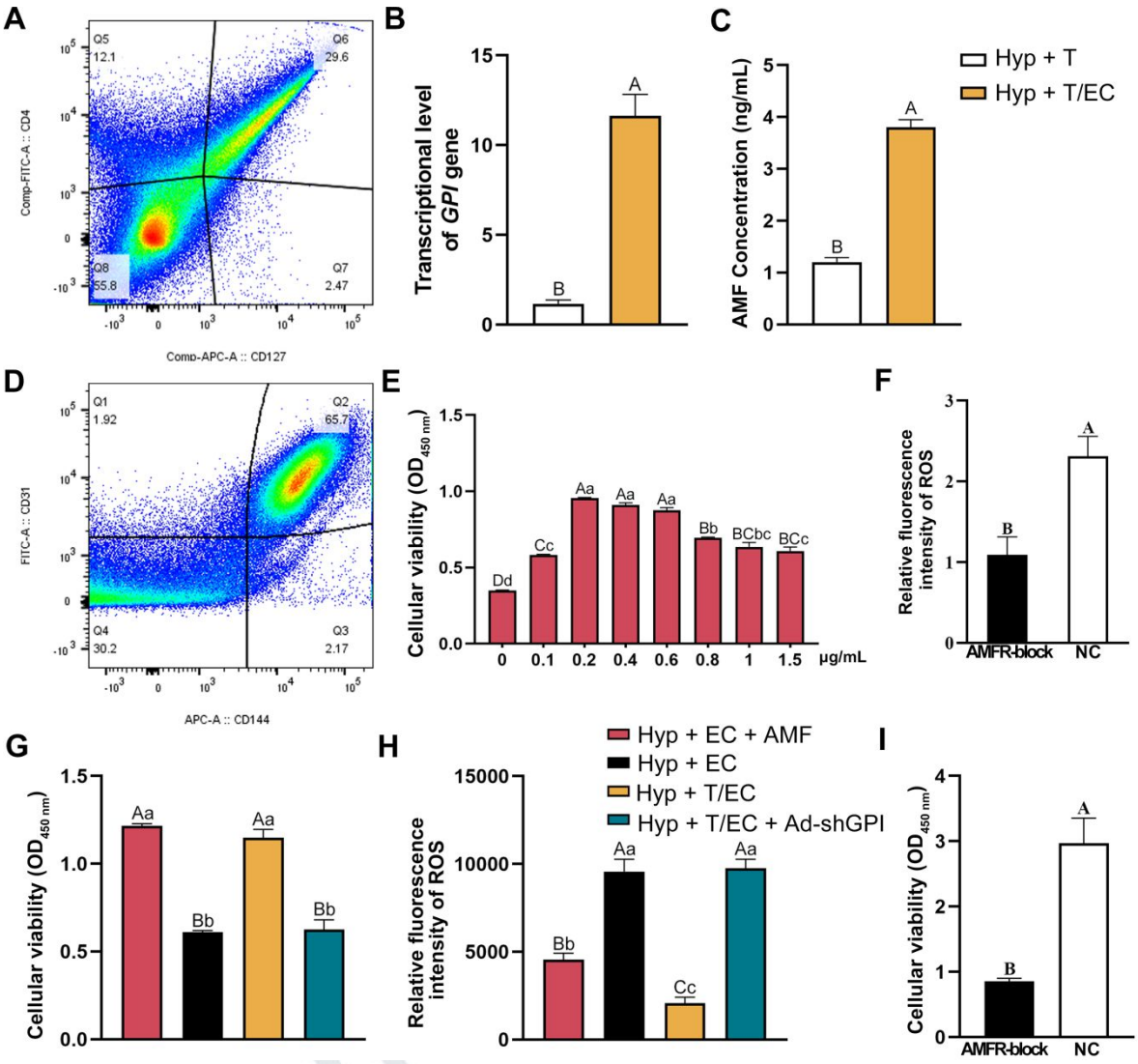


Figure 5. The CD4 *ATF7IP*$^+$ subtype (T) facilitates hypoxic adaptation of gCap subtype (EC) via the GPI/AMF−AMFR signaling axis

(**A**) Flow cytometric sorting strategy for the CD4 *ATF7IP*$^+$ subtype. The hierarchical gating was defined as Zombie$^-$/CD45$^+$/CD3$^+$/CD4$^+$/CD127$^+$. (**B**) GPI/AMF mRNA transcription level in CD4 *ATF7IP*$^+$ subtype under hypoxia during monoculture and co-culture with gCap subtype, with groups coloured as indicated in the legend to Figure 5C. Hyp: hypoxia model; T/EC: co-culture of CD4 *ATF7IP*$^+$ and gCap subtypes. Data are presented as mean (SEM). Different uppercase and lowercase letters between groups indicate $P<0.01$ and $P<0.05$, respectively. (**C**) Concentration of GPI/AMF in the culture supernatant of CD4 *ATF7IP*$^+$ subtype under hypoxia during monoculture and co-culture with the gCap subtype, with groups coloured as indicated in the legend. (**D**) Flow

Zoological Research

cytometric sorting strategy for the gCap subtype. The hierarchical gating was defined as Zombie$^-$/CD45$^-$/CD31$^+$/CD144$^+$. (**E**) Dose-dependent effects of recombinant AMF protein on the viability of the yak gCap subtype. Data are presented as mean (SEM), with statistical notation as described in Figure 5B. (**F**) Relative ROS fluorescence intensity of the gCap subtype following treatment with an AMFR-blocking antibody compared to the control group. Statistical notation follows that described in Figure 5B. (**G**) Cell viability of the gCap subtype under different treatments, with groups coloured as indicated in the legend to Figure 5H. Hyp: hypoxia model; T/EC: co-culture of CD4 *ATF7IP*$^+$ and gCap subtypes; AMF: recombinant GPI/AMF protein treatment; Ad-shGPI: adenoviral GPI/AMF knockdown. Statistical notation follows that described in Figure 5B. (**H**) Relative ROS fluorescence intensity in the gCap subtype under different treatments, with groups coloured as indicated in the legend. (**I**) Cell viability of the gCap subtype following treatment with an AMFR-blocking antibody compared to the control group.

uncorrected proof

中文标题

一种牦牛中富集的新型 CD4 *ATF7IP*$^{+}$细胞亚型：参与低氧条件下肺血管内皮细胞应激抵抗

作者

曾睿琳[1,3,7,#]，付伟[2,3,#]，张强[4,#]，余大为[5]，王嘉博[3]，徐孟[2,3]，殷实[3]，吉文汇[2,3]，熊燕[3]，泽让东科[6]，李键[1,3]，巴桑旺堆[4]，兰道亮[1,2,3,*]

[1]西南民族大学，青藏高原动物遗传资源保护与利用教育部重点实验室，四川成都 610041

[2]西南民族大学，青藏高原研究院，四川成都 610225

[3]西南民族大学，畜牧兽医学院，四川成都 610041

[4]西藏自治区农牧科学院，畜牧兽医研究所，西藏拉萨 850004

[5]中国农业科学院北京畜牧兽医研究所，农业农村部动物遗传育种与繁殖国家重点实验室，北京 100193

[6]西南民族大学，草地资源学院，四川成都 610225

[7]郑州大学，生命科学学院，河南郑州 450001

*通讯作者：兰道亮，landaoliang@163.com

摘要

阐明高原低氧环境适应的调控机制，是遗传学领域面临的一项重要挑战。牦牛高度适应青藏高原生态环境，而肺脏在气体交换和机体血氧稳态维持过程中发挥着关键作用。为探究低氧条件下肺脏的细胞组成及分子调控网络，本研究构建了牦牛、犏牛和黄牛的肺脏单细胞转录组图谱。本研究共鉴定出 51 种细胞亚型，其中包括 13 种新发现的亚型，这些新亚型主要富集于 T&NK 细胞群。通过整合物种间差异分析、拟时序分析及 SCENIC 转录因子调控网络分析，我们鉴定出一种在牦牛中显著富集的 CD4 *ATF7IP*$^{+}$细胞亚型。该亚型的丰度在黄牛、犏牛和牦牛中呈逐级递增趋势，表明其可能是与牦牛高原低

uncorrected proof

Zoological Research

氧适应相关的标志性细胞亚型。随后，细胞间通讯分析发现，CD4 *ATF7IP*$^{+}$亚型与肺脏毛细血管内皮细胞亚型（gCap）之间具有最强的配体–受体相互作用。进一步实验验证表明，由 CD4 *ATF7IP*$^{+}$亚型分泌的 GPI/AMF（自分泌运动因子）可与其受体 gp78（又称 AMFR）发生相互作用。该 AMFR 介导的信号通路依赖 PI3K 的磷酸化过程，进而促进 AKT 激活，有助于抑制活性氧（ROS）的积累，并维持低氧条件下肺脏 gCap 内皮细胞的存活。此外，在低氧条件下对 gCap 亚型给予重组 GPI/AMF 蛋白处理，也能够重现上述保护效应，并在一定程度上等效与 CD4 *ATF7IP*$^{+}$细胞共培养所产生的作用。综上，本研究揭示了一条此前尚未被认识的肺脏免疫细胞—血管内皮细胞调控轴，该调控轴有助于增强 gCap 内皮细胞在低氧条件下的应激抵抗能力，为进一步阐明高原低氧适应性机制奠定了基础，同时也为牦牛种质资源保护及定向选育提供了潜在的分子靶点。

uncorrected proof